

Dynamical Blueprints for Galaxies

Lawrence M. Widrow¹

*Department of Physics, Engineering Physics, and Astronomy, Queen's University,
Kingston, ON, K7L 3N6, Canada*

Brent Pym²

*Department of Mathematics, University of Toronto, 40 St. George Street, Toronto, ON,
M5S 2E4, Canada*

John Dubinski³

*Department of Astronomy and Astrophysics, University of Toronto, 60 St. George Street,
Toronto, ON, M5S 3H8, Canada*

(submitted to the Astrophysical Journal, October, 2007)

ABSTRACT

We present an axisymmetric, equilibrium model for late-type galaxies which consists of an exponential disk, a Sersic bulge, and a cuspy dark halo. The model is specified by a phase space distribution function which, in turn, depends on the integrals of motion. Bayesian statistics and the Markov Chain Monte Carlo method are used to tailor the model to satisfy observational data and theoretical constraints. By way of example, we construct a chain of 10^5 models for the Milky Way designed to fit a wide range of photometric and kinematic observations. From this chain, we calculate the probability distribution function of important Galactic parameters such as the Sersic index of the bulge, the disk scale length, and the disk, bulge, and halo masses. We also calculate the probability distribution function of the local dark matter velocity dispersion and density, two quantities of paramount significance for terrestrial dark matter detection experiments.

¹widrow@astro.queensu.ca

²bpym@math.toronto.edu

³dubinski@astro.utoronto.ca

Though the Milky Way models in our chain all satisfy the prescribed observational constraints, they vary considerably in key structural parameters and therefore respond differently to non-axisymmetric perturbations. We simulate the evolution of twenty-five models which have different Toomre Q and Goldreich-Tremaine X parameters. Virtually all of these models form a bar, though some, more quickly than others. The bar pattern speeds are $\sim 40 - 50 \text{ km s}^{-1} \text{ kpc}^{-1}$ at the time when they form and then decrease, presumably due to coupling of the bar with the halo. Since the Galactic bar has a pattern speed $\sim 50 \text{ km s}^{-1} \text{ kpc}^{-1}$ we conclude that it must have formed recently.

Subject headings: Galaxy: kinematics and dynamics — methods: statistical — methods: N-body simulations — cosmology: dark matter

1. INTRODUCTION

Dynamical galactic models serve a variety of purposes. They may be used to interpret the structural and kinematical observables of galaxies – surface brightness profiles, rotation curves and velocity dispersion profiles – in terms of intrinsic three-dimensional density and velocity distributions. Dynamical models also provide a starting point for controlled simulations of complicated processes such as the formation of bars and spiral structure. In short, galactic modeling provides the essential interface between observations and detailed theories of galaxy formation.

In this paper, we introduce a new dynamical model for late-type galaxies which comprises a disk, bulge, and dark halo. The model is derived from equilibrium solutions to the collisionless Boltzmann and Poisson equations. It is extremely flexible and may be tailored to satisfy observational data and theoretical constraints. We use Bayesian statistics and the Markov Chain Monte Carlo (MCMC) method to implement these constraints and to determine the probability distribution function (PDF) of the model in the full multi-dimensional parameter space.

Our model builds upon earlier work by Kuijken & Dubinski (1995) and Widrow & Dubinski (2005). The original Kuijken & Dubinski model consists of an exponential disk, a King-model bulge, and a lowered Evans-model halo and has the attractive feature that the phase space distribution function (DF) is built from analytic functions of the integrals of motion. No additional assumptions about the velocity-space distribution are made. By contrast, the widely-used approach described in Hernquist (1993) (see also Springel & White (1999)) assumes that the local velocity distributions of the halo and bulge particles are Gaussian with disper-

sions estimated from the Jeans equations. This approach leads to models which are slightly out of equilibrium. When used as initial conditions in N-body experiments, they readjust to a different state from the one proposed (see, for example, Kazantzidis, Magorrian, & Moore (2004)).

There are two main disadvantages of the Kuijken and Dubinski models. First, the bulge and halo have constant density (or weakly cuspy) centers whereas actual bulges and dark halos may have central density cusps. Second, the structure of the bulge and halo are determined *implicitly* by the model parameters. (By construction, the disk’s structural parameters, namely its radial and vertical scale lengths, its mass, and its truncation radius, are determined explicitly by the model parameters.) Widrow & Dubinski (2005) built a galactic model with r^{-1} -density cusps for both the bulge and halo but again, with a DF that determines the structure of the bulge and halo implicitly.

For our new model, the closed-form DF is abandoned in favor of a numerical DF which is designed to yield, to a very good approximation, user-specified density profiles for the bulge and halo. That is, the density profiles of the bulge and halo are now *explicit* functions of the model parameters. The present version of the model allows for a Sersic bulge and a halo with $\rho \propto r^{-\gamma}$ as $r \rightarrow 0$ where γ is between 0 and 2.

Our model is specified in terms of fifteen or so parameters. How are these parameters selected? One approach is to choose models at random and identify the ones that satisfy certain general constraints (e.g., the Tully-Fisher and size-luminosity relations). The result would be a catalog of disk-bulge-halo systems which could be used to study kinematical and dynamical trends such as the circular speed-central velocity dispersion ($V_c - \sigma_0$) relation (see, for example, Couteau et al. (2007)). A catalog of this type could also be used for N-body studies of mergers or interactions between galaxies in a cosmological environment. A second approach, and the one pursued here, is to build models for specific galaxies. Following Kuijken & Dubinski (1995) and Widrow & Dubinski (2005), we use the Milky Way as our illustrative example.

Modeling the Milky Way is a time-honoured endeavor; notable examples include Innanen (1973), Clutton-Brock, Innanen, & Papp (1977), Bahcall & Soneira (1980), Caldwell & Ostriker (1981), Kuijken & Gilmore (1991), Rohlfs & Kreitschmann (1988), Malhotra (1995); Kochanek (1996), Evans & Wilkinson (1999), and Klypin, Zhao, & Somerville (2002). Our construction of dynamical Milky Way models is in the spirit of the mass model survey by Dehnen & Binney (1998). Their models comprise a multi-component disk, a bulge, and a halo and are characterized by ten parameters. Twenty-two examples are presented, each the result of a maximum likelihood analysis in which some parameters are held fixed while others are allowed to vary. The Dehnen & Binney likelihood function is constructed by comparing model predictions

with six sets of observational data: the inner and outer Galactic rotation curves, the Oort constants, the mass at large radii, the local vertical force, and the line-of-sight velocity dispersion in Baade’s window. The advantage of our models is that they not only describe the potential-density pair for the Galaxy but also, the underlying DF. We therefore have the ability to examine the stability of our Galactic models using N-body simulations, an issue that is often ignored (but see Sellwood (1985) and Fux (1997)).

For the most part, we adopt Dehnen & Binney’s choice of observational data though we include more complete observations of the line-of-sight dispersion in the bulge region as well as photometric data from the COBE satellite. We also present what we believe to be a more balanced treatment of the likelihood function. Most significantly, we bring to the problem the powerful tools of Bayesian statistics and MCMC. These tools allow us to map out PDFs of both input parameters and derived quantities.

Though our model represents an axisymmetric, equilibrium system, it is susceptible to non-axisymmetric instabilities and therefore provides a natural starting point for numerical studies of galactic dynamics. An N-body realization of the model can be easily generated from the DF and then used as the initial conditions for a numerical simulation.

The Milky Way models in our MCMC series all satisfy the observational constraints but vary considerably in their structural properties. We simulate a selection of twenty-five models which span a wide range in Toomre Q (Toomre 1964) and Goldreich-Tremaine X (Goldreich & Tremaine 1978, 1979) parameters and find that a bar develops in virtually all of the cases. The onset of the bar instability can occur immediately or after several Gyr, depending on the model.

We present the model in Section 2, review the observational constraints in Section 3, and provide a summary of the essentials of Bayesian statistics and the MCMC method in Section 4. We discuss some preliminaries including our choice of prior probabilities, in Section 5. We present the results of our MCMC analysis in Section 6 and the results of our bar formation simulations in Section 7. In Section 8 we summarize our main conclusions and speculate on how we might improve upon and extend the models and MCMC analysis.

2. GALACTIC MODELS

We consider axisymmetric, collisionless systems whose DF is of the form

$$f(\mathcal{E}, L_z, E_z) = f_{\text{disk}}(\mathcal{E}, L_z, E_z) + f_{\text{bulge}}(\mathcal{E}) + f_{\text{halo}}(\mathcal{E}) \quad (1)$$

where $\mathcal{E} \equiv -E$ is the relative energy, L_z is the angular momentum about the symmetry axis, and E_z is the energy associated with vertical motions of stars in the disk (Kuijken & Dubinski 1995; Widrow & Dubinski 2005). For time-independent, axisymmetric systems \mathcal{E} and L_z are integrals of motion while E_z is an approximate integral of motion for disk stars on nearly circular orbits. Jeans theorem implies that a system generated by equation 1 will be in approximate equilibrium.

Integrating equation 1 over all velocities yields the density in terms of the gravitational potential, Φ , and the cylindrical coordinates R and z :

$$\rho(R, z, \Psi) = \rho_{\text{disk}}(R, z, \Psi) + \rho_{\text{bulge}}(\Psi) + \rho_{\text{halo}}(\Psi) \quad (2)$$

where $\Psi \equiv -\Phi$ is the relative potential. (Note that implicit in equation 1 is the assumption that the bulge and halo velocity dispersions are isotropic.) Self-consistency requires that ρ and Ψ satisfy Poisson’s equation

$$\nabla^2 \Psi = -4\pi\rho(R, z, \Psi) \quad (3)$$

which is accomplished, in practice, through an iterative scheme. (Note that here and throughout, we set Newton’s constant $G = 1$.)

Kuijken & Dubinski (1995) chose f_{bulge} to be the King model DF (King 1966) and f_{halo} to be the lowered Evans model DF from Kuijken & Dubinski (1994). (The latter depends on L_z as well as \mathcal{E} thereby allowing for flattened halos.) Their models have two main shortcomings. First, bulges and halos may have central density cusps whereas the King and lowered-Evans DFs yield density profiles with constant-density cores. Second, the relationship between the model parameters and the density profiles of the bulge and halo is implicit rather than explicit and not particularly intuitive.

Widrow & Dubinski (2005) built galactic models with cuspy ($\rho \propto r^{-1}$ as $r \rightarrow 0$) bulges and halos. Specifically, they chose the Hernquist (1990) DF for the bulge and a DF from Widrow (2000) for the halo. The latter was constructed to yield the so-called NFW profile

$$\rho_{\text{NFW}}(r) = \frac{\rho_h}{(r/a_h)(1 + r/a_h)^2} \quad (4)$$

(Navarro, Frenk & White 1996). Widrow & Dubinski (2005) altered these DFs in an attempt to account for the gravitational potential of the other components though the modifications were somewhat *ad hoc*. Consequently, the density profile of the halo differed from the NFW profile and likewise for the bulge.

A further drawback of the Widrow & Dubinski (2005) model is that the Hernquist bulge and NFW halo are arguably too restrictive. The Hernquist DF yields a system whose surface

density profile is well approximated by the $R^{1/4}$ -law (de Vaucouleurs 1948). The bulges of late-type galaxies are found to have surface brightness profiles which follow the more general Sersic law,

$$\Sigma(r) = \Sigma_0 e^{-b(R/R_e)^{1/n}}, \quad (5)$$

with Sersic index n between 0.6 and 2 (Andredakic, Peletier, & Balcells 1995; Courteau, de Jong, & Broeils 1996). Likewise, dark matter halos may have density profiles more general than the NFW form. Since the work of Navarro, Frenk & White (1996), there has been considerable debate over the actual form of halo density profiles. Moore et al. (1999) find evidence in their simulations for steeper cusps ($\rho \propto r^{-1.5}$). More recently, Navarro et al. (2004) conclude that the logarithmic slope of the halo density profiles decreases steadily with radius though their results are still consistent with equation 4. On the observational front, the rotation curves of dark matter-dominated low surface brightness galaxies appear to favour constant density cores (Moore 1994; Flores & Primack 1994; McGaugh & de Blok 1998; van den Bosch et al. 2000) though this interpretation of the data is being challenged on a number of fronts.

For our new models, we begin by choosing target density profiles, $\tilde{\rho}_{\text{bulge}}$ and $\tilde{\rho}_{\text{halo}}$, for the bulge and halo. Assume, for the moment, that the system is spherically symmetric. Through the Abel integral transform,

$$f_i(\mathcal{E}) = \frac{1}{\sqrt{8\pi^2}} \int_0^{\mathcal{E}} \frac{d^2 \tilde{\rho}_i}{d\Psi_{\text{total}}^2} \frac{d\Psi_{\text{total}}}{\sqrt{\mathcal{E} - \Psi_{\text{total}}}} \quad i = \text{bulge or halo}, \quad (6)$$

(Binney & Tremaine 1987), we can construct bulge and halo DFs which yield the target density profiles. In the case of an isolated halo or bulge, Ψ_{total} is the potential derived from $\tilde{\rho}_{\text{halo}}$ or $\tilde{\rho}_{\text{bulge}}$ and equation 6 reduces to the usual expression for the DF of a spherically symmetric system with isotropic velocities. The DF for a system following the Sersic law was found with this method by Ciotti (1991). DFs for NFW halos were found by Zhao (1997), Widrow (2000), and Lokas & Mamon (2000). For a composite system or one with an external potential, one simply replaces the Ψ derived from $\tilde{\rho}_i$ with the total gravitational potential. Tremaine et al. (2002) used this method to derive DFs for bulges with central black holes by setting $\Psi_{\text{total}} = \Psi_{\text{bulge}} + GM_{\text{blackhole}}/r$.

Equation 6 is only valid for spherically symmetric systems, a condition violated once a disk is included. Our approach is to use a spherical approximation (essentially, the monopole term of a spherical harmonics expansion) for the disk potential in evaluating Ψ_{total} . We stress that equation 6 is used to construct $f_{\text{halo}}(\mathcal{E})$ and $f_{\text{bulge}}(\mathcal{E})$, not to solve for $\Psi(R, z)$ and $\rho(R, z)$. We can use $f_{\text{halo}}(\mathcal{E})$ and $f_{\text{bulge}}(\mathcal{E})$ in equation 1 even though the composite system is not spherically symmetric; A DF of the form $f = f(\mathcal{E})$ yields an equilibrium system in *any* time-

independent potential regardless of the spatial symmetries of the potential.¹ The bulge and halo of the final model are axisymmetric (but not spherically symmetric) since isodensity surfaces follow isopotential surfaces (equation 2), the latter being flattened by the disk. As we demonstrate below, the spherically-averaged density profiles of the bulge and halo are very close to the target profiles.

2.1. Target Density Profiles

We choose the target density profile for the bulge to be

$$\tilde{\rho}_{\text{bulge}}(r) = \rho_b \left(\frac{r}{R_e} \right)^{-p} e^{-b(r/R_e)^{1/n}} \quad (7)$$

which yields the Sersic law (equation 5) for the projected surface density profile provided one sets $p = 1 - 0.6097/n + 0.05563/n^2$ (Prugniel & Simien 1997; Terzić & Graham 2005). Note that here and in equation 5, Σ_0 , R_e and n are free parameters while the constant b is adjusted so that R_e encloses half the total projected light or mass. In our models, we use

$$\sigma_b \equiv (4\pi n b^{n(p-2)} \Gamma(n(2-p)) R_e^2 \rho_b)^{1/2} \quad (8)$$

rather than ρ_b to parametrize the overall density scale of the bulge models. With this definition, σ_b^2 corresponds to the depth of the gravitational potential associated with the bulge.

We choose the target density profile of the halo to be

$$\tilde{\rho}_{\text{halo}} = \frac{2^{2-\gamma} \sigma_h^2}{4\pi a_h^2} \frac{1}{(r/a_h)^\gamma (1+r/a_h)^{3-\gamma}} C(r; r_h, \delta r_h) \quad (9)$$

where C is a truncation function that smoothly goes from unity to zero at $r = r_h$ over a width δr_h . We use the function

$$C(r; r_h, \delta r_h) = \frac{1}{2} \text{erfc} \left(\frac{r - r_h}{\sqrt{2} \delta r_h} \right). \quad (10)$$

The halo profile is therefore characterized by five parameters: r_h , δr_h , the halo scale length, a_h , the velocity scale, σ_h , and the central “cusp strength”, γ . For $r < r_h$, the mass interior to radius r is given by

¹A *self-consistent* system with a DF that depends only on the energy must be spherically symmetric (Binney & Tremaine 1987). The statement in the text applies to systems in which there is an external potential that does not necessarily respect spherical symmetry. Here the potential due to the disk plays the role of an external potential to the halo and bulge.

$$M(r) = 2^{2-\gamma} \sigma_h^2 a_h \left(\frac{1}{1 + r/a_h} + \log(1 + r/a_h) \right) . \quad (11)$$

Following Kuijken & Dubinski (1995), we adjust the disk’s DF so that its space density falls off approximately exponentially in R and as sech^2 in z with radial and vertical scale lengths R_d and z_d respectively. The disk is truncated at a radius R_{out} with a truncation sharpness parameter δR_d . In addition, we choose a DF where the radial dispersion profile is approximately exponential:

$$\sigma_R^2(R) = \sigma_{R0}^2 \exp(-R/R_\sigma) . \quad (12)$$

For simplicity, we set $R_\sigma = R_d$ in accord with observations by Bottema (1993).

3. OBSERVATIONAL CONSTRAINTS

We use nine sets of observational data as constraints on our Milky Way models. Five of these data sets – the inner and outer rotation curves, the Oort constants, the vertical force in the solar neighborhood, and the total mass at large radii – are largely taken from Dehnen & Binney (1998) and references therein. We incorporate measurements of the line-of-sight bulge dispersion from the compilation of data by Tremaine et al. (2002) as well as estimates of the local velocity ellipsoid from Binney & Merrifield (1998). We also use dust-corrected near-infrared DIRBE data from the COBE satellite (Binney, Gerhard, & Spergel 1997).

- *Inner rotation curve*

Inside the solar circle, the Galactic rotation curve is usually presented in terms of the “terminal velocity”, the peak velocity along a given line-of-sight at Galactic coordinates $b = 0$ and $|l| < \pi/2$. Assuming that the Galaxy is axisymmetric, v_{term} is given by

$$v_{\text{term}} = v_c(R) - v_c(R_0) \sin l \quad (13)$$

where R_0 is the distance from the Sun to the Galactic center and v_c is the circular speed (see, for example, Binney & Merrifield (1998)). Following Dehnen & Binney (1998) we use data from HI emission observations by Malhotra (1995) restricted to the range $\sin l \geq 0.3$ so as to avoid distortions from the bar.

- *Outer rotation curve*

The radial velocity of an object relative to the local standard of rest, v_{lsr} , is related to the circular rotation curve through the equation

$$v_{\text{lsr}} = \left(\frac{R_0}{R} v_c(R) - v_c(R_0) \right) \cos b \sin l \quad (14)$$

where $R = (d^2 \cos^2 b + R_0^2 - 2R_0 d \cos b \sin l)^{1/2}$, (l, b) are the Galactic coordinates, and d is the distance to the object. Measurements of $v_{\text{lsr},i}$ and d_i are compared to model estimates for $W(R)$ and $d(R)$ where $W(R) \equiv (R_0/R) v_c(R) - v_c(R_0) \equiv v_{\text{lsr}}/\cos b \sin l$. R is regarded as a free parameter which is adjusted to minimize

$$\chi_i^2 = \left(\frac{W(R) - W_i}{\Delta W_i} \right)^2 + \left(\frac{d(R) - d_i}{\Delta d_i} \right)^2 \quad (15)$$

where $W_i \equiv v_{\text{lsr},i}/\cos b \sin l$. In what follows we use data from Brand & Blitz (1993) with the same restrictions as in Dehnen & Binney (1998) (i.e., $l \leq 155^\circ$ or $l \geq 205^\circ$, $d > 1$ kpc, and $W < 0$) so as to avoid contamination from non-circular motions.

- *Local circular speed*

A further constraint from the rotation curve of the Galaxy comes from estimates of the circular speed at the solar radius, $v_c(R_0)$. Here, we adopt the estimate of Reid et al. (1999) who carried out VLBA observations of Sgr A*. Under the assumption that Sgr A* is at the center of the Galaxy, they found

$$v_c(R_0) = (219 \pm 20 \text{ km s}^{-1}) \left(\frac{R_0}{8 \text{ kpc}} \right) \quad (16)$$

which is consistent with other other estimates (Sackett 1997).

- *Vertical force above the disk*

Kuijken & Gilmore (1991) use K dwarf stars as tracers of the gravitational potential above the Galactic plane thereby placing a constraint on the total surface density in the solar neighborhood. They find

$$\frac{|K_z(1.1 \text{ kpc})|}{2\pi G} = 71 \pm 6 M_\odot \text{pc}^{-2} \quad (17)$$

independent of the relative contributions of the disk and halo. By including additional constraints on the local circular speed, Galactocentric distance of the Sun, and Oort constants, one can ferret out the separate contributions of the disk and halo to the local surface density. Doing so, Kuijken & Gilmore (1991) found

$$\Sigma_{\text{disk}} = 48 \pm 9 M_{\odot} \text{pc}^{-2}, \quad (18)$$

in excellent agreement with estimates of known matter in the solar neighborhood. We adopt equation 17 as the constraint on the vertical force at $(R, z) = (R_0, 1.1 \text{ kpc})$ and equation 18 the constraint on the surface density of the disk at $R = R_0$.

- *Oort constants*

The Oort constants,

$$A \equiv \frac{1}{2} \left(\frac{v_c}{R} - \frac{\partial v_c}{\partial R} \right)_{R=R_0} \quad \text{and} \quad B \equiv -\frac{1}{2} \left(\frac{v_c}{R} + \frac{\partial v_c}{\partial R} \right)_{R=R_0}, \quad (19)$$

measure, respectively, the local shear and vorticity in the Galactic disk. Here we adopt the constraints

$$A = 14.8 \pm 0.8 \text{ km s}^{-1} \text{ kpc}^{-1} \quad B = 12.4 \pm 0.6 \text{ km s}^{-1} \text{ kpc}^{-1} \quad (20)$$

from the Feast & Whitelock (1997) analysis of Cepheid proper motion measurements by the Hipparcos satellite.

- *Local velocity ellipsoid*

The kinematics of stars in the solar neighborhood provide important constraints on the structure of the Milky Way. The observation that $\overline{v_R^2} \neq \overline{v_z^2}$ already tells us that the disk DF necessarily involves a third integral of motion (Binney 1987). Our constraints for the local velocity ellipsoid are taken from Table 10.4 of Binney & Merrifield (1998) which in turn were derived from Edvardsson et al. (1993). Binney & Merrifield (1998) give separate values for the thin and thick disks. Since our models assume a single disk component we use a mass-weighted average (Widrow & Dubinski 2005).

- *Bulge dispersion*

Observations of the line-of-sight velocity dispersion in the direction of the bulge provide important constraints on the bulge parameter and, to a lesser extent, the parameters of the other components. We use measurements of the line-of-sight dispersion between 4 pc and 1300 pc from the compilation by Tremaine et al. (2002). Since the bulge is triaxial, the measured line-of-sight dispersion depends on the observer's orientation to its principal axes. Our line-of-sight to the Galactic center is approximately 20° from the long axis of the bulge (Binney, Gerhard, & Spergel 1997) and therefore the measured line-of-sight dispersion will be systematically higher than the values one would obtain assuming a spherical bulge. Following Tremaine et al. (2002), we adjust the measured dispersions downward by a factor 1.07 to account for this effect.

- *Mass at large radii*

The observed velocity distribution of the Milky Way satellite system and the dynamics of the Magellanic Stream, together with measurements of the high-velocity tail of the local stellar velocity distribution, provide constraints on the large-scale mass distribution of the Galactic halo. Following Dehnen & Binney (1998), who base their arguments on analyses by Kochanek (1996) and Lin, Jones, & Klemola (1995), we adopt

$$M(r < 100 \text{ kpc}) = (7 \pm 2.5) \times 10^{11} M_{\odot} \quad (21)$$

as a constraint on the mass distribution at large radii.

- *Surface photometry*

The distribution of stars in the Milky Way is most easily determined from observations in the near infrared where stellar emission dominates over dust emission. Though dust is more transparent at these wavelengths than in the optical, extinction due to dust is still significant toward the Galactic center. Spergel, Malhotra, & Blitz (1996) produced extinction-corrected maps of the inner Galaxy based on the DIRBE data set and a three-dimensional dust model (see also Freudenreich (1998)). Binney, Gerhard, & Spergel (1997) constructed three-dimensional models for the light distribution of the disk and bulge based on these maps with the aim of constraining the structural parameters of the Galactic bar.

Our initial goal is to construct axisymmetric models for the Galaxy. Toward this end, we use the surface brightness as a function of l at mid Galactic-latitudes ($3^{\circ} < |b| < 4.5^{\circ}$) from Binney, Gerhard, & Spergel (1997) (their Figure 2, lower panel) where the effects of the bar are not so pronounced (i.e., where their axisymmetric model adequately reproduces the observed surface brightness profile).

The mass model survey of Dehnen & Binney (1998) employs a maximum likelihood analysis where the likelihood function is $\exp(-\chi_{\text{DB}}^2)$ with

$$\chi_{\text{DB}}^2 = \frac{W_{\text{in}}}{N_{\text{in}}} \chi_{\text{in}}^2 + \frac{W_{\text{out}}}{N_{\text{out}}} \chi_{\text{out}}^2 + \frac{W_{\text{other}}}{N_{\text{other}}} \chi_{\text{other}}^2 . \quad (22)$$

The subscripts “in”, “out”, and “other” refer to the inner and outer rotation curve constraints and the other constraints (e.g., Oort constants, vertical force) respectively. The N_i are the numbers of data points actually used while W_i are weights introduced by Dehnen & Binney (1998) to account for “the number of really independent constraints”. That is, the W_i are meant to compensate for the fact that a quantity such as the Oort constant A has been

obtained from a large number of data points. Dehnen & Binney (1998) choose $W_{\text{in}} = W_{\text{out}} = W_{\text{other}} = 6$ though admit that the choice of W_i ’s are “subject to ones prejudices”.

In our view, the likelihood function should be $\exp(-\chi_{\text{tot}}^2/2)$ where

$$\chi_{\text{tot}}^2 = \chi_{\text{in}}^2 + \chi_{\text{out}}^2 + \chi_{\text{other}}^2 . \quad (23)$$

The fact that the Oort constant constraints are obtained from a large number of (raw) data points is already accounted for by the small quoted errors. Dividing χ_{in}^2 by N_{in} unfairly short-changes the rotation curve data in favour of the Oort constant constraints, and so forth.

To survey the model parameter space, Dehnen & Binney (1998) adopt the following approach; fix certain parameters and maximize the likelihood function by allowing the remaining parameters to vary. The procedure is then repeated with the fixed parameters set to different values, or different subsets of parameters held fixed. The result is a rather uneven survey of the full parameter space. A similar exercise was carried out by Widrow, Perrett, & Suyu (2003) for M31 using the original Kuijken and Dubinski models together with rotation curve, velocity dispersion, and surface brightness data. This procedure was also used for both M31 and the Milky Way in Widrow & Dubinski (2005). Bayesian statistics and MCMC provide a more complete picture of the model parameter space as we now demonstrate.

4. BAYESIAN ANALYSIS AND MCMC

Our aim is to calculate the posterior probability density function, $p(M|D, I)$, of a Galactic model M given data D and prior information I . M is specified by the fifteen model parameters as well as additional astronomical parameters – here R_0 and the mass-to-light ratios of the disk and bulge, $(M/L)_d$ and $(M/L)_b$. We collect the parameters into a vector \mathbf{A} with components A^j where $j = 1..N$ and N is the total number of parameters. From Bayes’ theorem

$$p(M|D, I) = \frac{p(M|I)p(D|M, I)}{p(D|I)} \quad (24)$$

where $p(M|I)$ is the prior probability density, $p(D|M, I)$ is the likelihood function, and $p(D|I) \equiv \int p(M|D, I) d\mathbf{A}$ is a normalization factor. Our choice of priors is described in the next section.

MCMC is an efficient means of calculating $p(M|D, I)$ whereby one constructs a sequence or “chain” of models whose density in parameter space is proportional to the posterior PDF provided the chain is long enough to have fully explored all “important” regions of parameter

space. Marginalization – that is, integration over a subset of parameters – is trivial; simply project the chain onto the appropriate subspace and compute the density of points. Likewise, the PDF of any model-dependent quantity is obtained by making a histogram of the quantity over the chain of models.

Our Markov chain is constructed via the Metropolis-Hastings algorithm (Metropolis et al. 1953; Hastings 1970) as outlined in Gregory (2005). The chain of models is described by the sequence \mathbf{A}_i , $i = 0, 1, 2, \dots$. We begin with a starting point \mathbf{A}_0 . A candidate for \mathbf{A}_1 is chosen according to the *jumping rule* (also known as the *proposal distribution*), $q(\mathbf{A}_1|\mathbf{A}_0)$. \mathbf{A}_1 is accepted with probability equal to $\min\{1, r\}$ where

$$r \equiv \frac{p(\mathbf{A}_1|D, I) q(\mathbf{A}_0|\mathbf{A}_1)}{p(\mathbf{A}_0|D, I) q(\mathbf{A}_1|\mathbf{A}_0)}. \quad (25)$$

Otherwise, \mathbf{A}_1 is set equal to \mathbf{A}_0 . The process is then repeated for \mathbf{A}_2 .

The success of an MCMC analysis rests, by and large, on choosing a suitable jumping rule. If the step size from \mathbf{A}_n to a candidate for \mathbf{A}_{n+1} is too small, the chain will move slowly through parameter space. On the other hand, if the step size is too large, most attempts to find a new point in parameter space will fail. In either case, exploration of parameter space, often referred to as mixing, can require a prohibitively large amount of computing resources. Ideally, the jumping rule is shaped like the PDF but scaled by a factor $2.4/\sqrt{N}$ (Gelman, Carlin, Stern, & Rubin 1995) which explains why it is often referred to as the proposal distribution.

In this work, we take q to be a multivariate Gaussian so that

$$\mathbf{A}_{n+1} = \mathbf{A}_n + \mathbf{D} \cdot \mathbf{G} \quad (26)$$

where \mathbf{G} is a vector of length N whose components are Gaussian random variables with unit variance and \mathbf{D} is a user-specified $N \times N$ matrix. Since neither \mathbf{D} nor \mathbf{G} depend on the model parameters, $q(\mathbf{A}_{n+1}|\mathbf{A}_n) = q(\mathbf{A}_n|\mathbf{A}_{n+1})$ and therefore $r = p(\mathbf{A}_{n+1}|D, I)/p(\mathbf{A}_n|D, I)$

We begin with a simple ansatz for the proposal distribution in which \mathbf{D} is a diagonal matrix whose non-zero elements are given by our best guess for the variance of each of the model parameters multiplied by $2.4/\sqrt{N}$. From a short chain of a few thousand models we estimate the covariance matrix

$$C_{ij} = \frac{\langle (A^i - \bar{A}^i)(A^j - \bar{A}^j) \rangle}{\langle A^i \rangle \langle A^j \rangle} \quad (27)$$

where $\langle \dots \rangle$ denotes an average along the chain. Our improved expression for the proposal distribution is given by equation 26 with $\mathbf{D}^2 = (2.4^2/N) \mathbf{C}$.

Each “data point” carries with it a quoted error. Of course, the observer may have underestimated the error or there may be features in the data which cannot be explained by the model. Both situations can be handled by introducing an unknown error parameter for each data set which is added in quadrature to the quoted error (Gregory 2005). For the purpose of the MCMC calculation, these error parameters are simply incorporated into an expanded definition of \mathbf{A} , that is, treated as model parameters.

5. PRELIMINARIES AND PRIORS

Simple arguments, based on general features of the Galaxy, provide preliminary estimates for the model parameters which in turn guide our choices of the prior probabilities used in the MCMC analysis. We assume that the priors for each of the model parameters are non-zero over a range somewhat larger than the range suggested by these estimates. For parameters that correspond to a physical scale (e.g., R_e , M_d , v_h) we assume a Jeffrey prior, essentially, equal probability in logarithmic intervals over the prescribed range. For dimensionless parameters, such as the halo cusp strength and Sersic index, we assume a flat prior. (See Gregory (2005) for a discussion.)

The projected velocity dispersion profile toward the Galactic bulge, $\sigma_p(R)$, reaches a peak value of $\sim 130 \text{ km s}^{-1}$ at a radius $\sim 200 \text{ pc}$ (Tremaine et al. 2002). On the other hand, estimates of the half-light or effective radius of the bulge, R_e , range from 570 pc to 920 pc (see Tremaine et al. (2002) and references therein).

The projected velocity dispersion of the Prugniel & Simien (1997) profile exhibits a similar structure to that of the Milky Way: $\sigma_p(R)$ is non-zero at $R = 0$, rises to a peak value of σ_{peak} at a radius R_{peak} and then decreases with radius (see Figure 10 of Prugniel & Simien (1997) as well as earlier work by Binney (1980) and Ciotti (1991)). The dimensionless ratios R_{peak}/R_e , $\sigma_{\text{peak}}/\sigma_b$ and $M_{\text{bulge}}/\sigma_b^2 R_e$ are functions of n as shown in Figure 1. From the figure we deduce that for the Milky Way, n is less than 2, R_e is between 0.57 kpc and 0.92 kpc , σ_b is between 340 km s^{-1} and 400 km s^{-1} , and M_b is between $1 \times 10^{10} M_\odot$ – $3.4 \times 10^{10} M_\odot$.

Binney, Gerhard, & Spergel (1997) constructed a model for the luminosity density of the Galaxy to fit data from the DIRBE experiment. Their model consisted of a triaxial bulge and double exponential disk with bulge-to-total luminosity ratio of 0.16. Subsequently, Malhotra, et al. (1995) derived a total L-band luminosity for the Milky Way of $7.1 \times 10^{10} L_\odot$ with $1.1 \times 10^{10} L_\odot$ attributed to the bulge.

Stellar population synthesis models provide estimates for the stellar mass-to-light ratios in different wavebands (Bell & de Jong (2001) and references therein). The L-band stellar

mass-to-light ratio for the disk is expected to be in the range $0.5\text{--}0.65$ in solar units (de Jong 2007) assuming a scaled Salpeter IMF (Bell & de Jong (2001)) and the Pegase population synthesis model. The mass-to-light ratio for the bulge could be somewhat higher. On the other hand, since our model does not include a separate gas disk, the effective mass-to-light ratio for the disk must account for any gas and should therefore be higher than the value for a pure stellar disk. The local stellar-to-gas ratio is ~ 1.6 (see Table 1 of Binney & Tremaine (1987)) and therefore the effective $(M/L)_d$ might be closer to 1. Together with our estimate for the disk luminosity, we conclude that M_d is between 3×10^{10} and $6 \times 10^{10} M_\odot$.

Reid (1993) reviewed estimates of the distance from the Sun to the Galactic center and concluded that $R_0 = 8.0 \pm 0.5$ kpc. More recently Eisenhauer et al. (2003) observed the star S2 in orbit about the Galaxy’s massive central black hole using the ESO VLT and found $R_0 = 7.94 \pm 0.42$ kpc.

Sackett (1997) reviewed estimates of the radial scale length of the Galactic disk and found $R_d = 3.0 \pm 1$ kpc. More recent estimates show a similarly large spread in values. Zheng et al. (2001) found $R_d = 2.75 \pm 0.3$ kpc from HST observations of M dwarfs while López-Corredoira et al. (2002) found $R_d = 3.3^{+0.5}_{-0.4}$ kpc from an analysis of old stellar populations using 2MASS survey data. As emphasized by Sackett (1997), the ratio R_0/R_d is observationally more secure than R_d . The estimates collected in her review show R_0/R_d between 2.7 and 3.5.

The disk scale height parameter, h_d , is more difficult to constrain since the Galactic disk comprises at least three distinct components, the gas disk, the thin disk, and the thick disk whereas our model has a single-component disk. Multi-component disks will be incorporated into future versions of the model but for the time being, h_d must represent the vertical mass distribution of all disk-like components. From Sackett (1997) we surmise that h_d is between 0.2 and 1 kpc.

The radial velocity dispersion in the solar neighborhood is $36 \pm 5.4 \text{ km s}^{-1}$ (Binney & Merrifield 1998). Together with estimates of the radial scale length of the disk and with equation 12, this translates into a range of possible values for σ_{R0} .

We allow the halo parameters to vary over a wide range of values. For example, we assume that the prior probability distribution of γ is uniform between 0 and 1.5 and non-zero otherwise. An alternative approach is to use cosmological models of halo and galaxy formation to guide one’s choice of the halo parameters (see, for example, Valenzuela & Klypin (2003)), but given uncertainties in the exact nature of adiabatic compression, variations among halo profiles found in different simulations, and possible discrepancies between halo profiles as inferred from observations and those found in simulations, we take a more conser-

vative approach. Furthermore, since the data do not probe the Galaxy beyond 100 kpc we set $r_h = 100$ kpc and $\delta r_h = 5$ kpc though no physical meaning should be ascribed to these values; r_h can be increased without changing the fit to the data.

Our choices for the prior probabilities of the model parameters are found in Table 1. In addition to the parameters listed in Table 1, we include unknown error parameters (see previous section) for the terminal velocity, outer rotation curve, bulge dispersion, and surface brightness profile data sets. Thus, our MCMC analysis is run with seventeen parameters.

6. MCMC RESULTS

We generate five Markov chains of length 2×10^4 . Each chain has roughly 3400 distinct members corresponding to an acceptance rate of 17%. We can calculate the PDFs for different quantities using the five chains individually and in combination. If mixing has been achieved then the results will be the same to within statistical uncertainties. In Figure 2 we illustrate that this is indeed the case by plotting the average values with 1σ error-bars for the a selection of six model parameters calculated for each of the five chains. For convenience, the values are normalized by dividing by the overall average.

6.1. Selected Models

In Figure 3 we show the rotation curve and density profile for a model from our MCMC series with $n \simeq 1$ and $\gamma \simeq 1$. Also shown are the target bulge and halo profiles (equations 7 and 9). We see that the model profiles are very close to the target ones. By comparison the halo profiles in the Widrow & Dubinski models differ significantly from the target (NFW) profile (see Figure 2, top panel, of Widrow & Dubinski (2005)).

We display results for the surface brightness profile (Figure 4), the terminal velocity (Figure 5), and the bulge line-of-sight velocity dispersion (Figure 6) for three models from our MCMC analysis. We choose models with $\gamma \simeq 1$ and Sersic parameters $n \simeq 0.6, 1$ and 2 . We also include a model with $n = 4$, that is, with essentially an $R^{1/4}$ -law bulge. Since our MCMC run does not find any models with a Sersic parameter this large we generate this model by fixing $n = 4$ and allowing the remaining parameters to vary.

While suitable models are found for n between 0.6 and 2 this is not the case for $n = 4$. This result is in agreement with studies of bulges in late-type spiral galaxies (Andredakic, Peletier, & Balcells 1995; Courteau, de Jong, & Broeils 1996; MacArthur, Courteau, & Holtz 2003) and suggests that the Galaxy has a pseudo-bulge rather than a classical bulge (see

Kormendy & Kennicutt (2004) for a review).

The models clearly have a difficulty reproducing the shape of the line-of-sight velocity dispersion profile. In particular, the local velocity minimum found in the data at $R \simeq 3$ pc is much deeper than is allowed by the models. The discrepancy may indicate that the density profile of the Galactic bulge is significantly different from the one proposed by Prugniel & Simien (1997) or that velocity-space anisotropy and deviations from spherical symmetry are necessary to model the dispersion profile in the innermost region of the bulge (Spergel, Malhotra, & Blitz 1996; Fux 1997; Freudenreich 1998).

6.2. Statistical Overview

The maximum *a posteriori* values and boundaries of the 68.3% credibility regions for the input parameters and calculated quantities are given in Tables 2 and 3 respectively. Not surprisingly, a_h and γ exhibit the largest fractional uncertainties. Most of the data used in this study pertains to the region of the Galaxy near and inside the Sun’s orbit about the Galactic center; Equation 21 provides a rather weak constraint on the mass at large radii (or equivalently, the circular speed at these radii). We note that a_h and γ are correlated in the sense that models with larger values of a_h have γ closer to 1 — large constant-density cores ($\gamma \simeq 0$ and $a_h \simeq 20 - 30$ kpc are disfavored by the data).

In Figure 7 we show the PDFs for the disk and bulge masses as well as the halo mass within 10 kpc and 100 kpc. We also show the pseudo-likelihood function for the twenty-two models considered in Dehnen & Binney (1998). Specifically, we plot

$$\mathcal{L}_{DB} = e^{-(\chi_{DB}^2 - \chi_{\min}^2)} \quad (28)$$

where χ_{DB}^2 is from their Table 3 with χ_{\min}^2 set to the value for their best-fit model. Our results for the disk, bulge, and halo masses are consistent with those of Dehnen & Binney (1998). Figure 7 illustrates the advantages of the MCMC method. The Dehnen & Binney analysis involves twenty-two separate maximum-likelihood calculations characterized by the authors’ *ad hoc* choices of fixed and free parameters. MCMC, on the other hand, yields the full multi-dimensional posterior probability function from which PDFs for one or more parameters are easily obtained.

Figure 8 provides a contour plot of the PDF in the $R_0 - R_d$ plane. Our results are consistent with previous estimates of these two quantities. The plot also shows the general trend that models with higher values of R_d tend to favor higher values of R_0 .

In Figure 9 we show the PDFs for n and γ . As noted above, our analysis clearly favours

bulges with surface brightness profiles closer to an exponential than to de Vaucouleurs $R^{1/4}$ -law. Our results allow for a dark halo with a wide range of inner logarithmic density slopes which includes the NFW value as well as steeper and shallower indices.

6.3. Comparison with Published Milky Way Models

In Figure 10, we compare values for the disk and bulge masses from our Markov chain analysis with those from a number of popular Milky Way models. One of the earliest mass models was constructed by Bahcall, Schmidt, & Soneira (1983). While they focus on constraining the Galactic spheroid through star counts (see also Bahcall & Soneira (1980)) they also fit the Galactic rotation curve by modeling the mass distribution of the disk, bulge, and dark halo. Their choice for the disk and bulge masses ($M_d = 5.6 \times 10^{10} M_\odot$ and $M_b = 1.1 \times 10^{10} M_\odot$) is represented in Figure 10 by the solid triangle.

From Shuttle IRT observations, Kent, Dame, & Fazio (1991) derived total K-band luminosities for the disk and bulge of $L_d = 4.9 \times 10^{10} L_\odot$ and $L_b = 1.1 \times 10^{10} L_\odot$, respectively. (Note that these values differ slightly from the values quoted in the original paper because a different value for the K magnitude of the Sun is used. Kent (1992) went on to construct disk-bulge-halo mass models based on these results and was able to fit the Galactic rotation curve for three choices of the disk mass-to-light ratio: a maximal disk model ($(M/L)_d = 1.3$), a high disk model ($(M/L)_d = 1.0$), and a low disk model ($(M/L)_d = 0.68$). In each case, the bulge mass-to-light ratio was $(M/L)_b = 1.0$. Kent’s models are shown in Figure 10 as blue, red, and green stars.

Klypin, Zhao, & Somerville (2002) constructed models for the Milky Way and Andromeda galaxies based on cosmologically motivated theories of disk formation. Their favored model for the Milky Way has $M_d = 4.0 \times 10^{10} M_\odot$ and $M_b = 0.8 \times 10^{10} M_\odot$ and is represented in Figure 10 by the solid square.

Since its discovery (Ibata, Gilmore, & Irwin 1994, 1995), the Sagittarius dwarf galaxy has held the promise of providing useful constraints on the size and shape of the Milky Way’s dark halo. The usual approach is to simulate the tidal disruption of Sagittarius as it passes through the Galactic potential and compare the distribution of tidal debris with photometric and kinematic observations of the observed tidal streams (see Law, Johnston, & Majewski (2005) for a recent example and references to earlier work). Johnston et al. (1999) introduced a model for the Galactic potential which has now become a standard for work in this area. The Johnston et al. (1999) values, $M_d = 1.0 \times 10^{11} M_\odot$ and $M_b = 3.4 \times 10^{10} M_\odot$, are shown in Figure 10 as an open square.

Our models occupy a smaller region of $M_d - M_b$ parameter space than is spanned by popular models from the literature. The Johnston et al. (1999) choices for M_d and M_b are inconsistent with our results by factors of 2.5 and 4, respectively. More to the point, their choices fall well outside the region of acceptable models. The choices for disk and bulge masses in Bahcall, Schmidt, & Soneira (1983) and Kent (1992) are consistent with our results as is the preferred model from Klypin, Zhao, & Somerville (2002).

6.4. *Implications for Dark Matter Detection Experiments*

Models of the Milky Way are an essential ingredient in the analysis of dark matter detection experiments. For example, microlensing experiments, which attempt to measure the distribution of massive compact halo objects (MACHOs) along various lines-of-sight through the halo, require a model for the MACHO component of the halo as well as the distribution of stars in the disk.

In analyzing their 5.7 year data set, the MACHO experiment considered a wide range of Galactic models (Alcock et al. 2000). Here we focus on their “standard model”. This model includes both a thin and thick disk, each with radial scale length $R_d = 4$ kpc and total disk mass is $M_d = 4.5 \times 10^{10} M_\odot$. The halo is modeled as a cored isothermal sphere with a density profile given by

$$\rho(r) = \rho_0 \frac{a^2 + R_0^2}{a^2 + r^2} \quad (29)$$

where, for their standard model, Alcock et al. (2000) assumed $R_0 = 8.5$ kpc, $a = 5$ kpc and $\rho_0 = 0.0079 M_\odot \text{pc}^{-3}$. Though they did not model the bulge explicitly, we can infer its mass through the requirement that the circular rotation speed of the Galaxy at $r = R_0$ is $\simeq 220 \text{ km s}^{-1}$. Doing so yields $M_b \simeq 2.6 \times 10^{10} M_\odot$ for their standard model (open triangle in Figure 10). Evidently, the bulge mass is inconsistent with our results by a factor of 3.

Terrestrial dark matter detection experiments aim to observe elementary particle dark matter candidates (e.g., WIMPs or axions) as they interact with a detector on Earth. These experiments are therefore sensitive to the local density and velocity distribution of dark matter particles. Estimates for the local dark matter density range from $0.005 - 0.02 M_\odot \text{pc}^{-3}$ ($0.2 - 0.8 \text{ GeV cm}^{-3}$) (See Bahcall, Schmidt, & Soneira (1983); Caldwell & Ostriker (1981); Turner (1986); Bergström, Ullio, & Buckley (1998)). The range quoted above is from Bergström, Ullio, & Buckley (1998) where a variety of halo profiles were considered.

We find (Table 3) $\rho_{\text{local}} = 0.0080 \pm 0.0014 M_\odot \text{pc}^{-3}$ and $\sigma_{\text{local}} = 240 \pm 23 \text{ km s}^{-1}$. The PDFs for these two quantities are plotted in Figure 8. Our values for the mean and lower bound for ρ_{local} are consistent with the values found in Bergström, Ullio, & Buckley (1998)

though our analysis suggests that their upper bound is too high by a factor of two. Our mean value for σ_{local} is lower than the standard value by about 30 km s^{-1} though the standard value still falls within the range of acceptable models. Our models tend to favour values for M_{100} at the low end of the range found in equation 21. Inspection of a scatter plot of models in the $M_{100} - \sigma_{\text{local}}$ plane reveals a clear correlation between the two quantities — models with values of M_{100} closer to the central in equation 21 have values of σ_{local} closer to the standard value.

6.5. Connection with Cosmology

Klypin, Zhao, & Somerville (2002) construct models for the Milky Way based on standard galaxy formation theory. In particular, they use model halos based on predictions from cosmological simulations with the further assumption that the halos undergo adiabatic contraction in response to the formation of the disk and bulge.

Though our MCMC analysis does not include cosmological constraints we can test whether our models are consistent with the standard cosmological paradigm *a posteriori*. To this end, we calculate the virial radius, R_{vir} , virial mass, M_{vir} , and concentration, c_{vir} , for all of the models in our MCMC series. By definition, the mean density inside R_{vir} is a factor Δ_{vir} greater than the background density, ρ_m . That is,

$$M_{\text{vir}} \equiv M(R_{\text{vir}}) \equiv \frac{4\pi}{3} \Delta_{\text{vir}} \rho_m R_{\text{vir}}^3 \quad (30)$$

where M_{vir} is the mass interior to R_{vir} . Δ_{vir} depends on the cosmological model; In what follows, we assume $\Omega_m \equiv \rho_m / \rho_{\text{crit}} = 0.3$ where $\rho_{\text{crit}} \equiv 3H^2/8\pi$ is the critical density and $H = 70 \text{ km s}^{-1} \text{ Mpc}$ (Tegmark et al. 2004). With these values, $\Delta_{\text{vir}} \simeq 340$ (Bryan & Norman 1998) (see also Bullock et al. (2001) and Wechsler et al. (2001)). The concentration, c_{vir} , is defined as the ratio of R_{vir} to the halo scale length R_s , the latter identified as the radius at which the logarithmic slope of the halo density profile equals -2. For a halo profile given by equation 9, $R_s = (2 - \gamma) a_h$.

In Figure 12, we show the PDF for our MCMC series projected onto the $M_{\text{vir}} - c_{\text{vir}}$ and $R_{\text{vir}} - c_{\text{vir}}$ planes. Also shown are the low-concentration, high-concentration, and favored models from Klypin, Zhao, & Somerville (2002). In the upper panels, R_{vir} , M_{vir} , and c_{vir} are calculated for the actual halos used in our models. The implication would seem to be that our models are more concentrated than the ones assumed in Klypin, Zhao, & Somerville (2002).

Recall, however, that Klypin, Zhao, & Somerville (2002) incorporate adiabatic contraction into their models. In order to compare our halos with theirs, we should assume

they too have undergone adiabatic contraction. We should therefore adiabatically “decontract” our halos and then calculate c_{vir} . We have done this using the usual assumptions (Blumenthal et al. 1986; Flores et al. 1993); The system is treated as being spherically symmetric. Initially, the baryons and dark matter are well-mixed. The baryons cool and form a disk and bulge while the halo particles respond adiabatically to the changing gravitational potential. Moreover, halo particles are assumed to follow circular orbits which do not cross as their orbits shrink. Under these assumptions, the quantity $rM(r)$ remains constant and one can calculate the initial radii of the dark matter particles given the final structure of the disk, bulge, and halo.

The results of this analysis are shown in the lower panels of Figure 12. Our models are now in excellent agreement with those found in Klypin, Zhao, & Somerville (2002).

Alam, Bullock, & Weinberg (2002) proposed $\Delta_{V/2}$, the mean density within the radius $R_{V/2}$ in units of ρ_{crit} , as a measure of the halo core densities. $R_{V/2}$ is defined as the radius at which the rotation curve reaches half its maximum value V_{max} . The quantity $(\Delta_{V/2}/8\pi^2)^{1/2}$ is equal to the number of rotation periods per Hubble time at the radius $R_{V/2}$. Alam, Bullock, & Weinberg (2002) found values of $\Delta_{V/2}$ in the range $5 \times 10^4 - 5 \times 10^6$ for dark matter-dominated galaxies, considerable scatter and no correlation between $\Delta_{V/2}$ and V_{max} .

The PDF for our MCMC series in the $\Delta_{V/2}-V_{\text{max}}$ plane is shown in Figure 13. The range of values for $\Delta_{V/2}$ is certainly consistent with those found in the Alam, Bullock, & Weinberg (2002) survey though some models have higher values — possibly reflecting that influence of baryons on the Milky Way’s dark halo. The considerable range indicates that the halo concentration is poorly constrained by the data used in our analysis.

7. BAR FORMATION

Near-IR photometry, gas and stellar kinematic measurements, and observations of gravitational microlensing events all strongly suggest that the Milky Way is a barred galaxy (see reviews by Kuijken (1996) and Gerhard (1996)). A bar represents a strong departure from axisymmetry and adds considerably to the challenge of modeling the Galaxy. A promising avenue is to use N-body simulations to follow the development of bars and spiral structure in an initially axisymmetric, equilibrium model. Ostriker & Peebles (1973) and Sellwood (1985) provide early examples of this approach. They were interested in stabilizing their Galactic models to avoid bar formation, the former proposing an unseen dark halo and the latter stressing the importance of the bulge. More recently, Fux (1997) attempted

to construct self-consistent models for the Milky Way’s bar by evolving unstable axisymmetric models and comparing the results with observations from the DIRBE experiment (Dwek, et al. 1995).

Bars, at least in idealized, initially-axisymmetric disk galaxies, form through swing amplification (Toomre 1981). (Whether bars in real galaxies form through this process or through some more complicated process during the formation of the galaxy itself is another matter.) In swing amplification, leading waves propagate outward and are amplified into trailing waves (and contained by the outer Lindblad resonance). Trailing waves then wind up. Within linear theory, if there is an inner Lindblad resonance (ILR), it absorbs the tightly wound trailing waves and thereby acts as a barrier preventing further growth. In the absence of an ILR, the trailing waves propagate through the center of the system and transform into leading waves. This feedback loop can lead to growth of a bar-like perturbation.

The Toomre Q (Toomre 1964) and Goldreich-Tremaine X (Goldreich & Tremaine 1978, 1979) parameters are the two most widely used diagnostic quantities for studying a galaxy’s resistance to the bar instability. Q measures the kinetic “temperature” of the disk; stellar disks with $Q < 1$ are unstable to local gravitational instabilities. X indicates a disk’s susceptibility to global instabilities. (X depends on the azimuthal mode number, m , of the perturbation. Here, we take $m = 2$ since we are interested in bars.) For disks with $X \lesssim 3$, the gain of the swing amplifier is large and bars are more likely to form. In general, the greater the contribution of the disk to the gravitational force felt by disk particles, the smaller the value of X .

Higher values of Q and X make a galaxy more resistant to the bar instability. The existence of an ILR barrier from a dense bulge or cuspy halo can also prevent the instability (Sellwood & Evans 2001). However, a bar can still form even if the galaxy initially has an ILR barrier. For example, interactions between halo substructure and the bulge or cusp may temporarily lower the ILR barrier and trigger bar formation in an otherwise stable galaxy (Gauthier, Dubinski, & Widrow 2006). Non-axisymmetric structure in the disk might also jostle the cusp and remove the ILR barrier, if only temporarily. In short, the notion of an ILR barrier assumes linear perturbation theory; non-linear disturbances may be able to overcome or disrupt the barrier and initiate the bar instability.

Our models provide a natural starting point for investigations of bar formation. The models generated by our MCMC run all yield acceptable fits to the observational data yet have very different stability properties. Figure 14 shows a contour plot of the model distribution in the $Q - X$ plane. (Of course, both Q and X are functions of radius. Here we use their minimum values.) Also shown is the distribution of models in the $X' - X$ plane

where

$$X' \equiv \frac{v_{\text{total}}^2(R)}{v_{\text{disk}}^2(R)_{R=2.2R_d}} \quad (31)$$

is a measure of the disk’s contribution to the gravitational force necessary to keep a particle in a circular orbit at a given radius. Here v_{total} is the circular rotation speed at cylindrical radius R and v_{disk} is the contribution to v_{total} from the disk (Debattista & Sellwood 1998, 2000). The radius $R = 2.2R_d$ is where v_{disk} reaches a maximum, assuming an exponential disk. The tight correlation between X and X' indicates these two quantities are interchangeable for most purposes.

We consider twenty-five models from our MCMC run which cover most of the area within the 95% likelihood contour in the $Q - X$ plane. The models in this study are depicted as dots in Figure 14 while their circular-speed curves are shown in Figure 15. In all cases, the circular speed reaches a peak value of approximately 220 km s^{-1} at a radius between $5 - 8 \text{ kpc}$ and then declines slowly.

Figure 16 shows the behavior of the functions Ω and $\Omega \pm \kappa/2$ where Ω is the angular velocity and κ is the epicyclic radial frequency. These functions should be compared with the pattern speed, Ω_p , of an emerging bar or spiral density wave. In particular, $\Omega = \Omega_p$ indicates the position of co-rotation while $\Omega_p = \Omega - \kappa/2$ indicates the position of the ILR. As we will see shortly, all of the bars that form in our simulations have initial pattern speeds in the range of $\sim 40 - 50 \text{ km s}^{-1} \text{ kpc}^{-1}$. Thus, about two thirds of the models in this study have initial ILRs. Note that in these cases, the rise in the $\Omega - \kappa/2$ -curve is very rapid and the radius of the ILR is only a few hundred parsecs.

Each of the twenty-five models depicted in Figure 14 are evolved for 5 Gyr using a parallelized treecode (Dubinski 1996). Simulations have 800K disk, 200K bulge, and 1M halo particles. The particle Plummer softening length is $\epsilon = 25 \text{ pc}$ and the simulations are run for 10^4 equal timesteps of length $\Delta t = 0.5 \text{ Myr}$. We generate surface density maps for the face on view of every tenth timestep and determine the strength and pattern speed of the bars that form. An animation depicting the evolution of the grid of simulations is available at <http://www.cita.utoronto.ca/~dubinski/DynamicalBlueprints/>

In Figure 17 we plot the amplitude of the bar-strength parameter

$$A_2 \equiv \frac{1}{N} \left| \sum_j e^{2i\phi_j} \right|, \quad (32)$$

as a function of time. Here ϕ_j is the usual azimuthal angle of the j^{th} disk particle and N is the total number of disk particles. All of the models form bars, with the possible exception of the $Q = 2, X = 4.5$ model (upper right-hand corner of the figures). Bars form almost

immediately in models with low values of Q and X . Indeed, the models in the lower left-hand region of the figures are violently unstable and radically transformed by both local and global instabilities. On the other hand, bars can take several billion years to form in models with higher values of Q and especially higher values of X .

Interestingly enough, the growth-rate of bars does not vary smoothly across the grid of models. In particular, models in the central column of the grid ($Q \simeq 1.5$) with higher values of X quickly develop bars. In general, these models have less massive and less dense bulges and no ILRs (see Figures 15 and 16). Hence, they are immediately vulnerable to Toomre’s swing amplification mechanism.

Virtually all of the models with ILRs eventually form bars though the onset of the instability is typically delayed. Two effects, one numerical and one physical, can lead to bar formation in the presense of an initial ILR. First, two-body relaxation may be important at radii near the ILR even with 10^6 halo particles. (Recall that in some models, the radius of the ILR can be as small as 100 pc.) As the central halo relaxes, the peak of the $\Omega - \kappa/2$ -curve can drop below the initial pattern speed. If this occurs, the ILR barrier disappears and the bar forms.

A second, more physical, explanation is that swing amplified spiral waves disturb the central region of the galaxy causing the ILR barrier to disappear, at least temporarily. Other non-linear disturbances, such as interactions between the disk and halo substructure, may also cause the ILR barrier to disappear. Simply put, the theory of the ILR barrier may not apply to situations where non-linear perturbations are present. We note that the importance of nonlinear effects for bar formation is discussed in Sellwood (1989).

The evolution of the bar length, R_b , and pattern speed, Ω_p , are shown in Figures 18 and 19. To estimate the bar length, we first construct the axis ratio profile of the isodensity contours for the disk. The axis ratio profile is defined to be the axis ratio, b/a , as a function of the semi-major axis, a . In general, b/a goes through a minimum with a typical value of $(b/a)_{\min} \simeq 0.4$ before rising abruptly in the transition from the end of the bar to the outer disk. As a heuristic measure of R_b we use the major axis length of the isodensity contour beyond the b/a -minimum and where $b/a \simeq 0.6$. The pattern speed is given by the time-derivative of the phase angle $\phi_0 = \tan^{-1}[\text{Im}(A_2)/\text{Re}(A_2)]/2$. We insure that ϕ_0 is sampled with enough time-resolution to avoid aliasing and to obtain a reasonable estimate of the pattern speed from $\Delta\phi/\Delta t$. In Figure 19, we show the pattern speed once the bar is easily detected above the noise.

Though the bars in our survey appear at different times, their initial pattern speeds are always in the range of $40 - 50 \text{ km s}^{-1} \text{ kpc}^{-1}$. Angular momentum transfer to the halo causes

Ω_p to decay to about $20 \text{ km s}^{-1} \text{ kpc}^{-1}$ over a few Gyr with the decay rate being slightly larger in models with higher mass halos. As expected, the bar lengths are generally less than the co-rotation radius though transient long bars with $R_b \approx 10 \text{ kpc}$ form in models with small Q and X before collapsing on themselves. For most models, bars grow monotonically in length as the pattern speed declines.

Bar formation alters the structure of the model and it is therefore natural to ask whether the evolved models still satisfy the original observational constraints. Though we will leave the details of such an analysis for future work, we include, in Figure 20, the evolution of the surface density profiles for our twenty-five simulated systems. We see that the surface density profiles of models with low values of Q and X are dramatically deformed; the redistribution of mass is so violent that the models almost certainly do not satisfy our observational constraints. On the other hand, models where the bar forms relatively late in the simulation show little evolution of the surface density profile. Their structure, at least in an azimuthally-averaged sense, remains largely unchanged.

The Galaxy is known to have a bar and estimates of its length and pattern speed can be compared with our results. Binney, Gerhard, & Spergel (1997) find $R_b = 3.5 \text{ kpc}$ and $\Omega_p \approx 60 - 70 \text{ km s}^{-1} \text{ kpc}^{-1}$ in their analysis of DIRBE photometry while Dehnen (1999) find a similar bar length but lower pattern speed ($\Omega_p = 53 \pm 3 \text{ km s}^{-1} \text{ kpc}^{-1}$) using the velocity distribution of solar neighborhood stars. Weiner & Sellwood (1999) model the gas kinematics of the inner galaxy and find $\Omega_p \approx 42 \text{ km s}^{-1} \text{ kpc}^{-1}$. The fact that nearly all of the models in our study are bar unstable and have initial pattern speeds near the range of the inferred values is promising. We note that certain models can be excluded such as those with very small values of Q and X . If we assume that the Galaxy’s bar has formed very recently than many of the models have the correct combination of bar length and pattern speed to match the observations. Furthermore, for larger Q and X , the change in the disk’s radial profile in response to the bar is small. These models may well provide a good barred model of the Galaxy. It should be noted that in all of these models, the pattern speed declines to $20 - 30 \text{ km s}^{-1} \text{ kpc}^{-1}$ within a few Gyr after the bar forms. *If we take these models seriously as reasonable facsimiles of the Galaxy, then we must conclude that Galactic bar formed within the last 1-2 Gyr.*

8. CONCLUSIONS

We have introduced a dynamical model for late-type galaxies that incorporates our current understanding of disk-bulge-halo systems. In particular, the bulge has a Sersic surface density profile and the halo has a central density cusp.

We have carried out an MCMC analysis of dynamical models for the Milky Way using a variety of kinematic and photometric constraints. The results are presented in the form of PDFs for both input parameters and derived quantities. The MCMC analysis provides a picture of the distribution of models in parameter space that is more complete than can be obtained by other approaches. Avoided is the awkward procedure of fixing a subset of parameters while allowing the remaining parameters to vary in some minimization scheme. Instead, a sequence of models is generated which contains all of the desired information. Marginalization over a subset of parameters is accomplished by simply projecting the model distribution onto the appropriate parameter subspace.

Our analysis suggests that the Milky Way has a pseudo-bulge with a Sersic index of 1.3 ± 0.3 . Our results for the masses of the disk, bulge, and halo are consistent with those of Dehnen & Binney (1998) but call into question choices for these quantities in some popular models from the literature. For example, the disk and bulge masses in Johnston et al. (1999) are entirely inconsistent with our results. The inferred bulge mass for the standard model used by the MACHO collaboration (Alcock et al. 2000) is inconsistent with our findings by a factor of 2.5. On the other hand, the standard values used by terrestrial dark matter detection experiments for the local dark matter density and velocity dispersion are consistent with our results.

A weak point of our analysis is the inability to tightly constrain the halo mass at large radii. Planetary nebulae, globular clusters, and satellite galaxies may be used as tracers of the Galactic potential. Dynamical models for the tracer populations are required to properly model kinematic data. In principle, it is straightforward to construct such models but there are subtle issues. Previous studies showed that velocity anisotropy in a tracer population can affect interpretation of kinematic data. Velocity anisotropy requires a DF that depends on at least one integral of motion in addition to the energy. The standard practice is to use the total angular momentum, L , but since our models include a disk, L is not conserved. (Previous analyses side-stepped this issue by using a spherically symmetric Galactic potential.)

Our MCMC analysis provides an ideal starting point for studies of disk stability and bar formation in that we have some 10^5 models, each of which can serve as initial conditions for a numerical experiment. We have performed a suite of simulations which focuses on the susceptibility of the disk to bar formation as a function of the stability parameters Q and X . Many of the models provide a good match to the inferred properties of the Galactic bar with the proviso that the bar has formed recently.

It is a pleasure to thank S. Courteau, S. Dodelson, R. de Jong, A. Graham, P. Gregory, S. Myers, D. Puglielli, J. Sellwood, D. Spergel, and A. Toomre for useful conversations. This

work was supported by the Natural Sciences and Engineering Research Council of Canada. Simulations were conducted on facilities funded by the Canadian Foundation for Innovation at the Canadian Institute for Theoretical Astrophysics.

REFERENCES

- Alam, S.M.K., Bullock, J. S., & Weinberg, D. H. 2002, *ApJ*, 572, 34
- Andredakis, Y. C., Peletier, R. F., & Balcells, M. 1995, *MNRAS*, 275, 874
- Alcock, C. 2000, *ApJ*, 542, 281
- Bahcall, J. N., Schmidt, M. & Soneira, R. M. 1983, *ApJ*, 265, 730
- Bahcall, J. N. & Soneira, R. M. 1980, *ApJS*, 44, 73
- Bell, E. F. & de Jong, R. S. 2001, *ApJ*, 550, 212
- Bergström, L., Ullio, P., & Buckley, J. H. 1998, *Astroparticle Physics*, 9, 137
- Bertone, G., Hooper, D., & Silk, J. 2004, *Physics Reports*, 405, 279
- Binney, J. 1980, 190, 873
- Binney, J., Gerhard, O., & Spergel, D. 1997, *MNRAS*, 288, 365
- Binney, J. 1987, in Gilmore, G. & Carswell, B. eds. *The Galaxy*, Reidel, Dordrecht, p. 399
- Binney, J., & Merrifield, M. 1998, *Galactic Astronomy*, Princeton Univ. Press, Princeton
- Binney, J., & Tremaine, S. 1987, *Galactic Dynamics*, Princeton Univ. Press, Princeton
- Blumenthal, G. et al. 1986, *ApJ*, 301, 27
- Bottema, R. 1993, *A&A*, 275, 16
- Brand, J. & Blitz, L. 1993, *A&A*, 275, 67
- Bryan, G. L. & Norman, M. L. 1998, *ApJ*, 495, 80
- Bullock, J. S. et al. 2001, *MNRAS*, 321, 559
- Caldwell, J. A. R. & Ostriker, J. P. 1981, *ApJ*, 251, 61
- Ciotti, L. 1991, *A&A*, 249, 91

- Clutton-Brock, M., Innanen, K. A., & Papp, K. A. 1977, *Ap&SS*, 47, 299
- Courteau, S., de Jong, R. S., & Broeils, A. H. 1996, *ApJ*, L73
- Courteau, S., McDonald, M., Widrow, L. M., & Holtzman, J., 2007, *ApJ*, 655, L21
- Debattista, V. P. & Sellwood, J. A. 1998, 493, L5
- Debattista, V. P. & Sellwood, J. A. 2000, 543, 704
- Dehnen, W. & Binney, J. 1998a, *MNRAS*, 294, 429
- Dehnen, W. 1999, *ApJ*, 524, L35
- de Jong, R. S., *private communication*
- de Vaucouleurs, G. 1948, *Ann. d’Astrophys.*, 11, 247
- Dwek, E. et al. 1995, *ApJ*, 445, 716
- Dubinski, J. 1996, *New Astronomy*, 1, 133
- Edvardsson et al. 1993, *A&A*, 275, 101
- Eisenhauer, F. et al. 2003, *ApJ*, 579, L121
- Evans, N. W., & Wilkinson, M. I. 1999, *MNRAS*, 310, 645
- Feast, M. W. & Whitelock, P. A., 1997, *MNRAS*, 291, 683
- Flores, R. et al. 1993, *ApJ*, 412, 443
- Flores, R. A. & Primack, J. R. 1994, *ApJ*, 427, L1
- Freudenreich, H. T. 1998, *ApJ*, 492, 495
- Fux, R. 1997, *A&A*, 327, 983
- Gauthier, J.-R., Dubinski, J., & Widrow, L. M. 2006, *ApJ*, 653, 1180
- Gelman, A., Carlin, J. B., Stern, H. S., & Rubin, D. B. 1995, *Bayesian Data Analysis*, Chapman & Hall, London
- Gerhard, O. E. 1996, in Blitz, L. & Teuben, P. (eds.), *Unsolved Problems of the Milky Way*, IAUS 169, 76
- Goldreich, P & Tremaine 1978, *ApJ*, 222, 850

- Goldreich, P & Tremaine 1978, ApJ, 233, 857
- Gregory, P. 2005, Bayesian Logical Data Analysis for the Physical Sciences, Cambridge University Press, UK
- Hastings, W. K. 1970, Biometrika, 57, 97
- Hernquist, L. 1990, ApJ, 356, 359
- Hernquist, L. 1993, ApJS, 86, 389
- Ibata, R. A., Gilmore, G., & Irwin, M. J. 1994, Nature, 370, 194
- Ibata, R. A., Gilmore, G., & Irwin, M. J. 1995, MNRAS, 277, 781
- Innanen, K. A. 1973, Ap&SS, 22, 393
- Johnston, et al. 1999, AJ, 118, 1719
- Kazantzidis, S., Magorrian, J., & Moore, B. 2004, ApJ, 601, 37
- Kent, S. M. 1992, ApJ, 387, 181
- Kent, S. M., Dame, T. M., & Fazio, G. 1991, 378, 131
- King, I. R. 1966, AJ, 71, 64
- Klypin, A., Zhao, H., & Somerville, R. S. 2002, ApJ, 573, 597
- Kochanek, C. S. 1996, ApJ, 457, 228
- Kormendy, J. & Bender, R. 1999, ApJ, 522, 772
- Kormendy, J. & Kennicutt, R. C. 2004, ARA&A, 42, 603
- Kuijken, K., & Dubinski, J. 1994, MNRAS, 269, 13
- Kuijken, K., & Dubinski, J. 1995, MNRAS, 277, 1341
- Kuijken, K., & Gilmore, G. 1991, ApJ, 367, L9
- Kuijken, K. 1996, in Ruta, R. et al., (eds.) Barred Galaxies, ASP Conference Series, 91, 504
- Law, D. R., Johnston, K. V., & Majewski, S. R. 2005, ApJ, 619, 807
- Lin, D. N. C., Jones, B. F., & Klemola, A. R. 1995, ApJ, 439, 652

- Lokas, E. L., & Mamon, G. A. 2000, MNRAS, 321, 155
- López-Corredoira et al. 2002, A&A, 394, 883
- Malhotra, S. 1995, ApJ, 448, 138
- Malhotra, S. et al. 1996, ApJ, 473, 687
- MacArthur, L. A., Courteau, S., & Holtzman, J. A. 2003, ApJ, 582, 689
- McGaugh, S. S. & de Blok, W. J. G. 1998, ApJ, 499, 41
- Metropolis, N. et al. 1953, Journal of Chemical Physics, 21, 1087
- Moore, B. 1994, Nature, 370, 629
- Moore, B. et al. 1999, MNRAS, 310, 1147
- Navarro, J. F., Frenk, C. S., & White, S. D. M. 1996, ApJ, 462, 563
- Navarro, J. F. et al. 2004, MNRAS, 349, 1039
- Ostriker, J. P., & Peebles, P. J. E. 1973, ApJ, 186, 467
- Press, W. H., Flannery, B. P., Teukolsky, S. A., & Vetterling, W. T. 1986, *Numerical Recipes*, (Cambridge: Cambridge University Press)
- Prugniel, P. & Simien, F. 1997, A&A, 321, 111
- Reid, M. J. 1993, ARA&A, 31, 345
- Reid, M. J. et al. 1999, ApJ, 524, 816
- Rohlf, K. & Kreitschmann, J. 1988, A&A, 201, 51
- Sackett, P. D., 1997, ApJ, 483, 103
- Sellwood, J. A. 1985, MNRAS, 217, 127
- Sellwood, J. A. 1989, MNRAS, 238, 115
- Sellwood, J. A., & Evans, N. W. 2001, ApJ, 546, 176
- Spergel, D. N., Malhotra, S. & Blitz, L. 1996, in *Spiral Galaxies in the Near-Infrared*, eds. D. Minniti & H.-W. Rix (Berlin: Springer) p. 128
- Springel, V. & White, S. D. M. 1999, MNRAS, 307, 162

- Tegmark, M. et al. 2004, Phys. Rev. D 69, 103501
- Terzić, B. & Graham, A. W. 2005, MNRAS, 362, 197
- Toomre, A. 1964, ApJ, 139, 1217
- Toomre, A. 1981, In: The structure and evolution of normal galaxies; Proceedings of the Advanced Study Institute, Cambridge University Press, 111
- Tremaine, S. et al. 2002, ApJ, 574, 740
- Turner, M. S. 1986, Phys. Rev. D, 33, 889
- Valenzuela, O. & Klypin, A. 2003 MNRAS, 345, 406
- van den Bosh, F. C. et al. 2000, AJ, 119, 1579
- Wechsler, R. H. et al. 2002, ApJ, 568, 52
- Weiner, B. J., & Sellwood, J. A. 1999, ApJ, 524, 112
- Widrow, L. M. 2000, ApJS, 131, 39
- Widrow, L. M., Perrett, & Suyu 2003, ApJ, 588, 311
- Widrow, L. M. & Dubinski, J., ApJ, 631, 838
- Zhao, H. 1997, 287, 525
- Zheng, Z. et al. 2001, ApJ, 555, 393

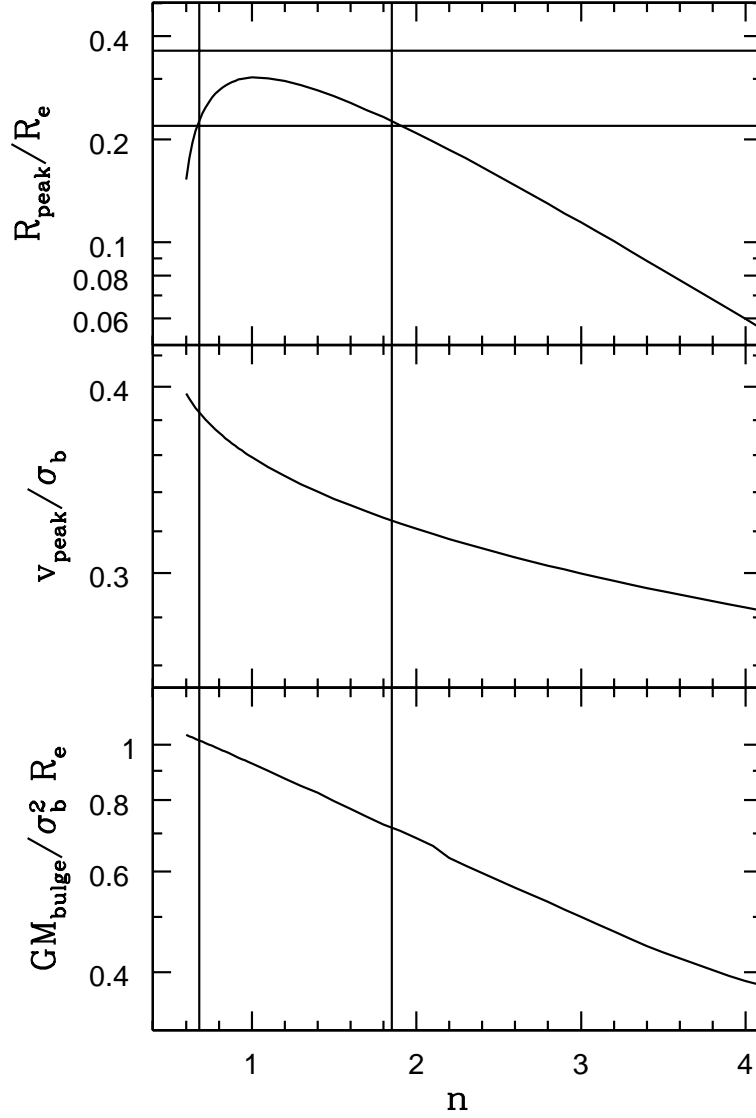


Fig. 1.— Characteristics of the line-of-sight velocity dispersion profile for the Prugniel & Simien (1997) density profile as a function of Sersic index n . The curve $\sigma_p(R)$ rises to a peak value of v_{peak} at a projected radius R_{peak} . Shown are the dimensionless ratios R_{peak}/R_e (upper panel), v_{peak}/σ_b (middle panel), and $GM_{\text{bulge}}/\sigma_b^2 R_e$ (lower panel) as functions of n . Data for the Galaxy compiled by Tremaine et al. (2002) suggest that R_{peak}/R_e lies in the range $0.22 - 0.36$ (horizontal lines). Vertical lines then delineate range of values for n .

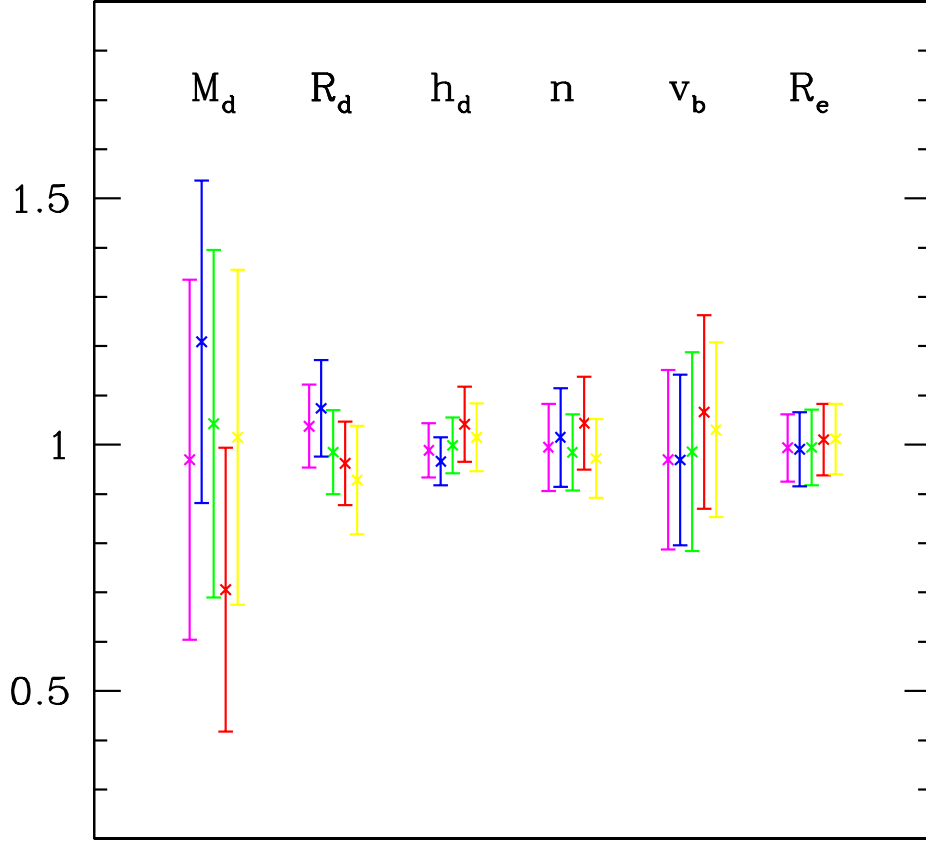


Fig. 2.— Average values and 1σ error bars for a selection of six model parameters as calculated from each of the five separate Markov chains. Values of the parameters are normalized by dividing by the overall average.

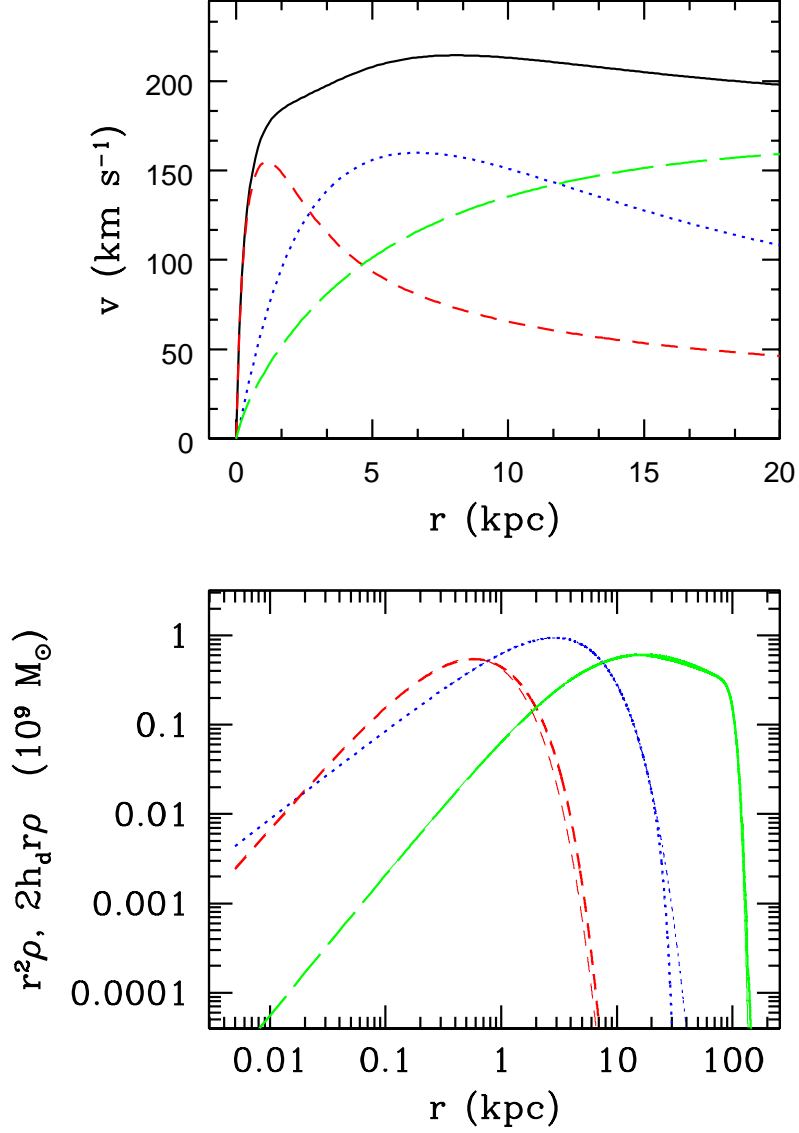


Fig. 3.— Rotation curve (top panel) and density profile (bottom) as a function of r for a model with $n \simeq 1$ and $\gamma \simeq 1$. Red (dashed) line is for the bulge; blue (dotted) line is for the disk; green (long-dashed) line is for the halo. In the top panel, the solid (black) line shows the total rotation curve. In the lower panel, we plot $r^2\rho$ for the bulge and halo and $h_d r\rho$ for the disk, quantities proportional to the mass in radial bins. Also shown in the lower panel (thin lines) are the “target” density profiles for the bulge and halo (equations 7 and 4 respectively).

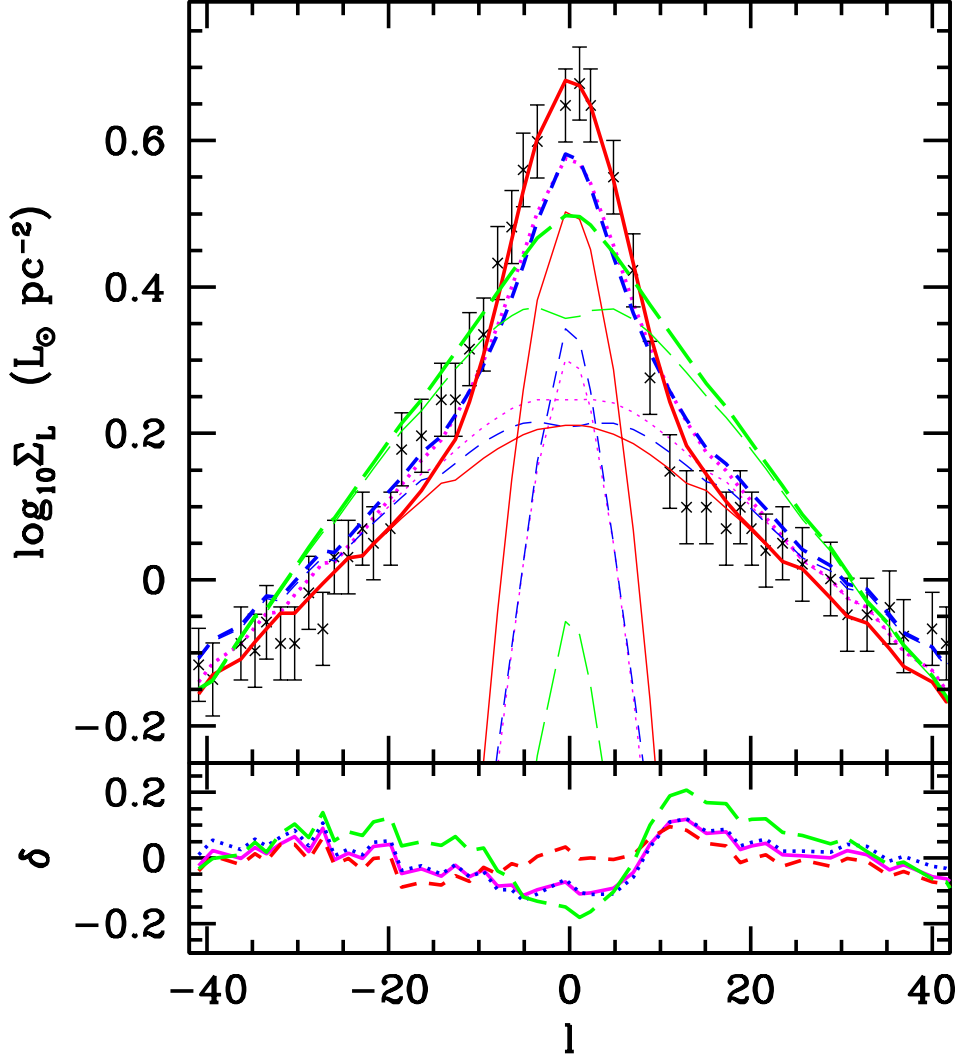


Fig. 4.— Surface brightness profile as a function of l for four models and for data from Spergel, Malhotra, & Blitz (1996). Three models are chosen from our main MCMC run: $(n, \gamma) \simeq (0.6, 1)$ — red curve; $(n, \gamma) \simeq (1, 1)$ — magenta curve; $(n, \gamma) \simeq (2, 1)$ — blue curve. Also shown (green curve) is a model chosen from a run where n is fixed to the “de Vaucouleurs” value, 4 and $\gamma = 0.86$. In the top panel, the thin curves show the separate contributions of the disk and bulge. Lower panel shows the residuals between the models and the data.

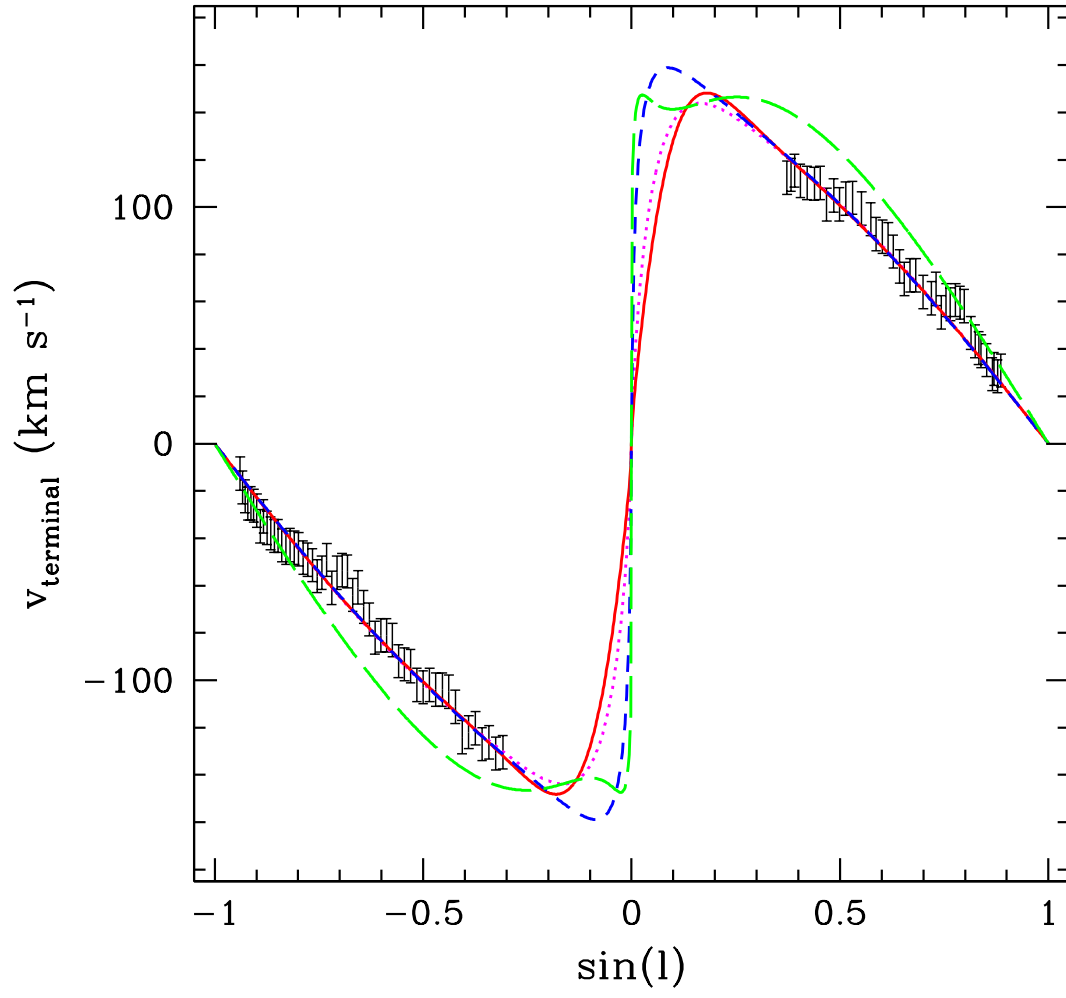


Fig. 5.— Terminal velocity as a function of $\sin l$ for four models and for data from Malhotra (1995). Line types and colours are the same as in Figure 4.

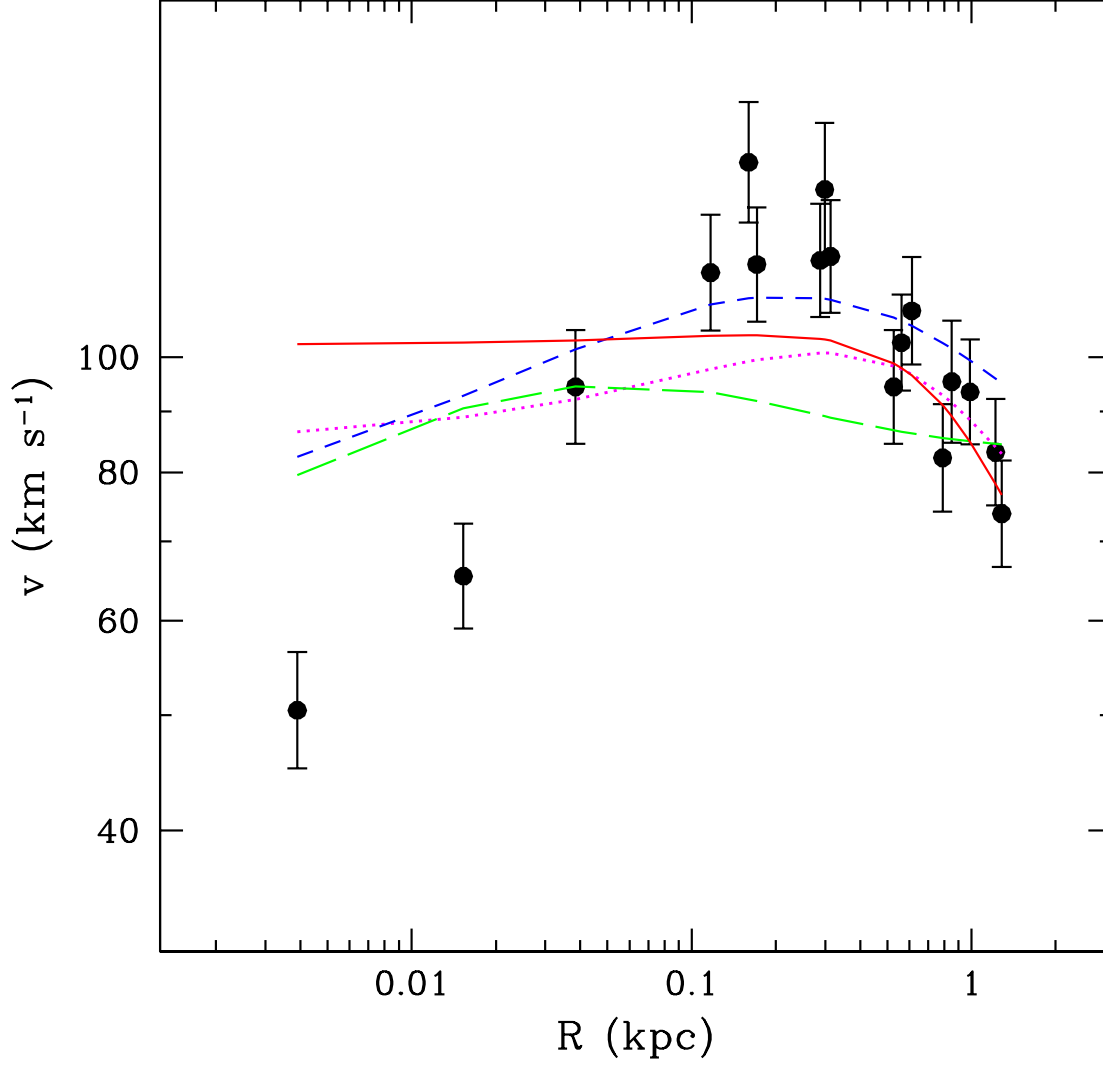


Fig. 6.— Line-of-sight velocity dispersion toward the bulge as a function of projected radius from the Galactic center for models and for data from Tremaine et al. (2002). Line types and colours are the same as in Figure 4.

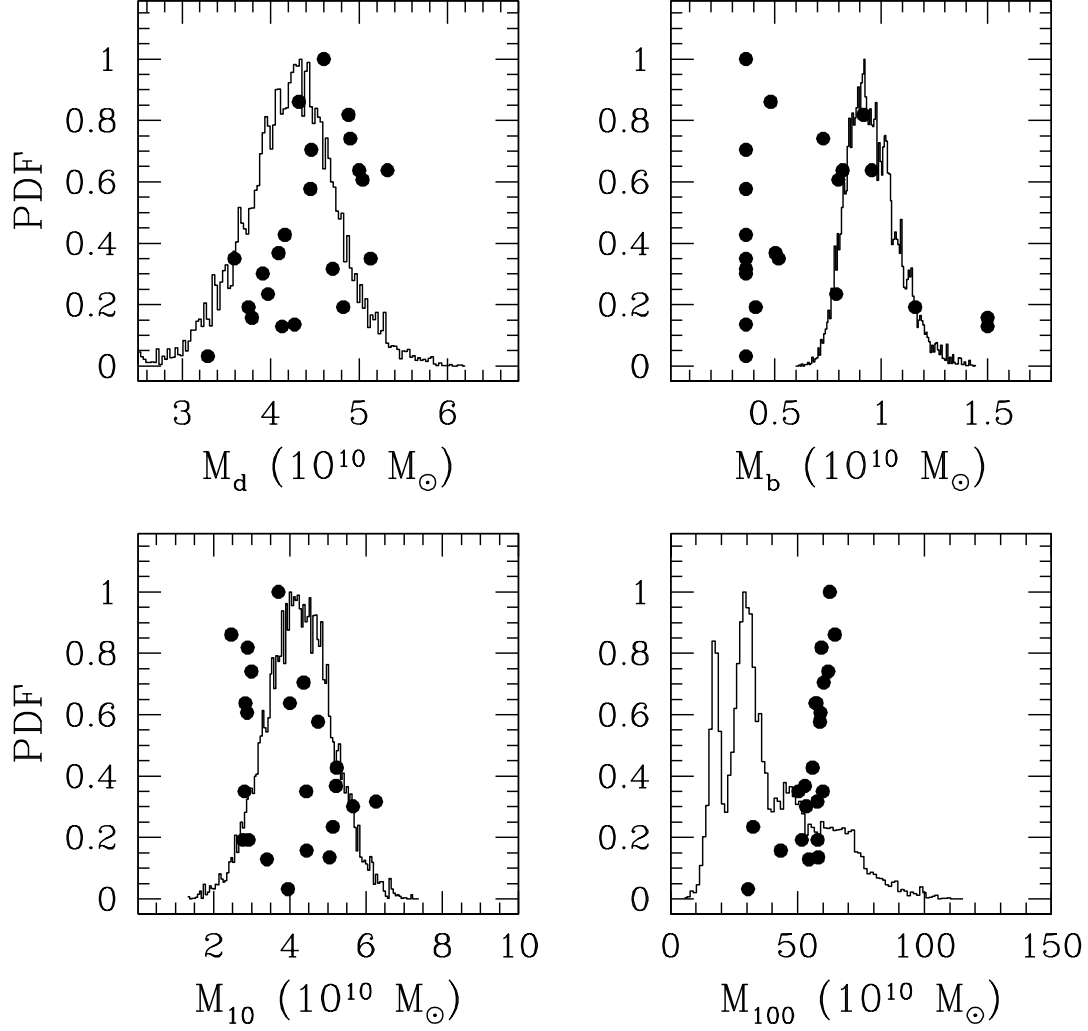


Fig. 7.— PDFs for the disk mass, bulge mass and halo mass within 10 and 100 kpc. Solid lines show results of the MCMC analysis. Dots show likelihood functions for the twenty-two models presented by Dehnen & Binney (1998).

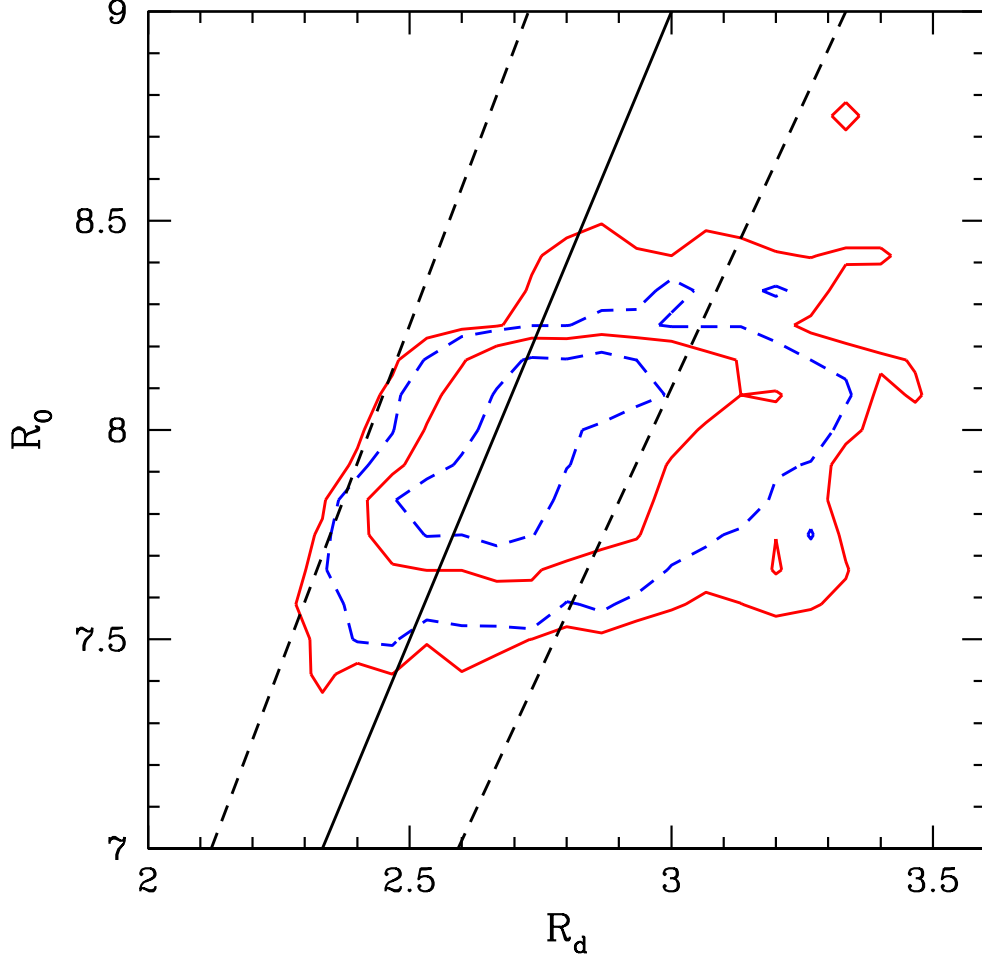


Fig. 8.— Contour plot of probability distribution function of models in the $R_0 - R_d$ plane. Solid contours enclose 68% and 95% of the models. Dashed contours enclose 38% and 87% of the models. The solid straight (black) line corresponds to $R_0/R_d = 3$. The dashed straight lines correspond to $R_0/R_d = 2.7$ and 3.3 .

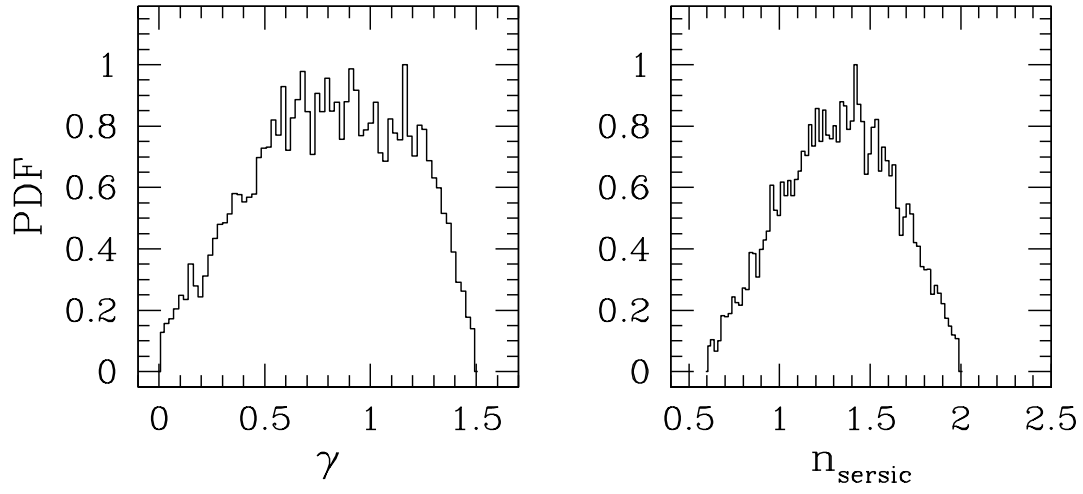


Fig. 9.— PDFs for the Sersic index, n , and cusp-strength parameter, γ .

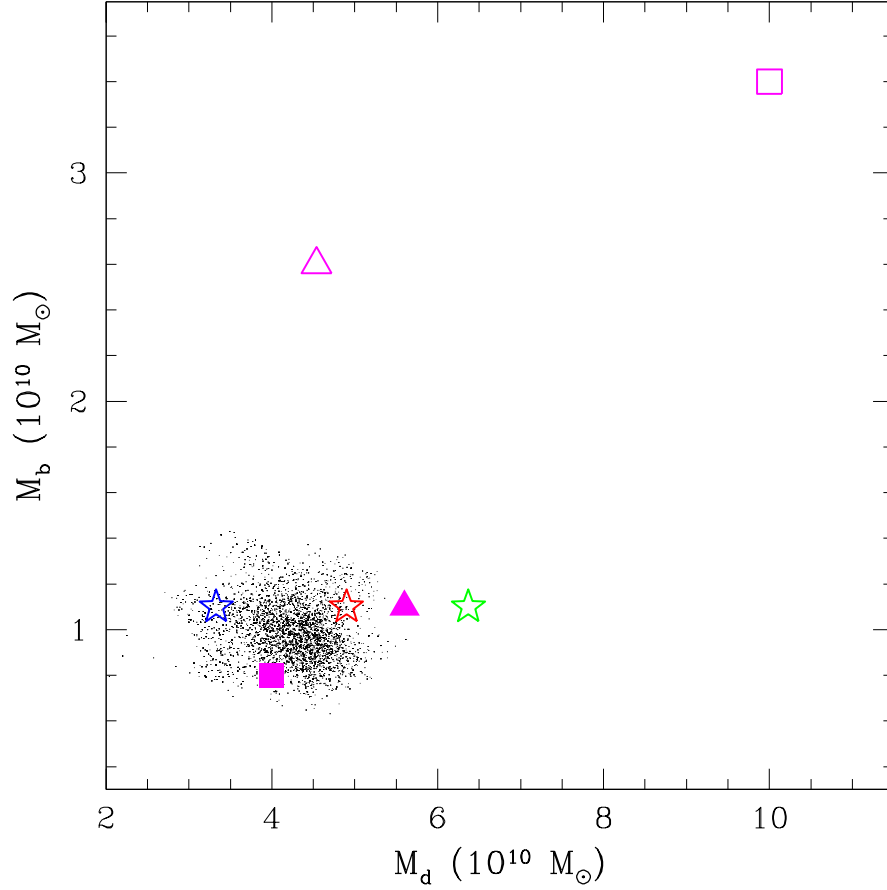


Fig. 10.— Comparison of our results for the disk and bulge mass with those from published Milky Way models. Cloud of points in the lower right corner are from the MCMC analysis. Stars from left to right (blue, red, green) represent, respectively, the low, high, and maximal models from Kent (1992). The filled triangle represents the model from Bahcall, Schmidt, & Soneira (1983) while the filled square represents the model from Klypin, Zhao, & Somerville (2002). The open square represents the model advocated by Johnston et al. (1999) in their studies of the tidal disruption of Sagittarius. The open triangle is the standard model adopted by the MACHO collaboration.

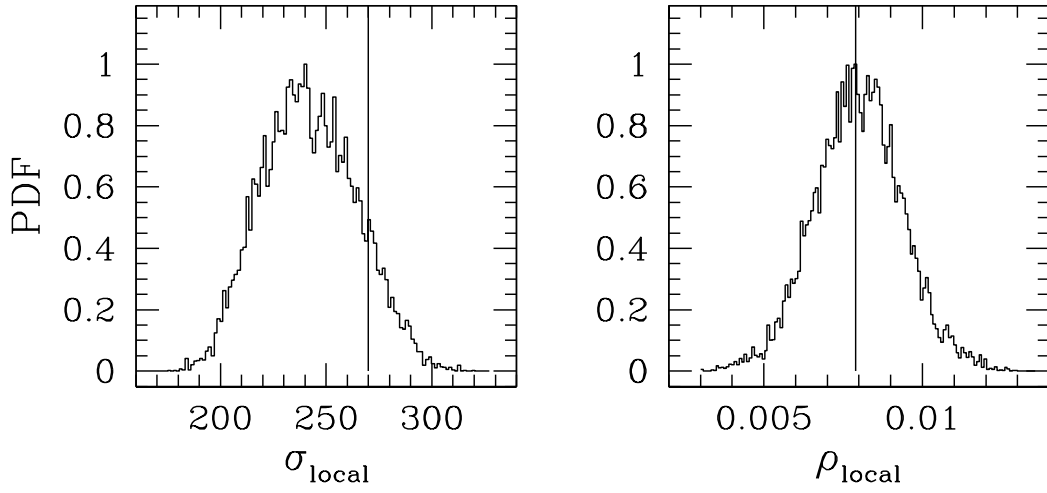


Fig. 11.— PDFs for the local dark matter velocity dispersion, σ_{local} and dark matter density, ρ_{local} . Vertical lines indicate the standard values assumed by most terrestrial dark matter detection experiments (see text).

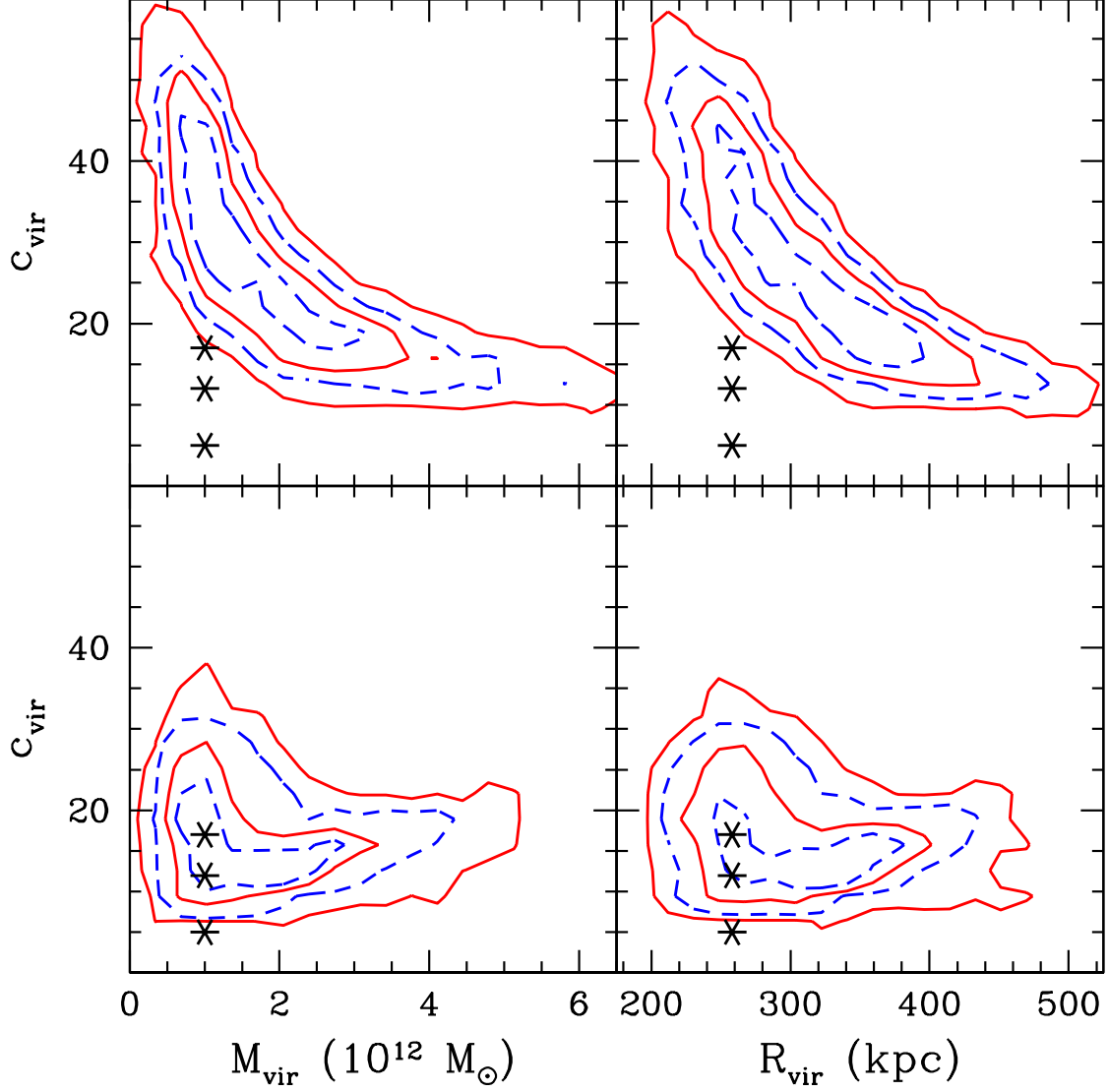


Fig. 12.— Contour plots of the probability distribution function of models in the $M_{\text{vir}} - c_{\text{vir}}$ and $R_{\text{vir}} - c_{\text{vir}}$ planes. Solid contours enclose 68% and 95% of the models. Stars indicate the favored, low-concentration ($c_{\text{vir}} = 5$) and high-concentration ($c_{\text{vir}} = 17$) models from Klypin, Zhao, & Somerville (2002).

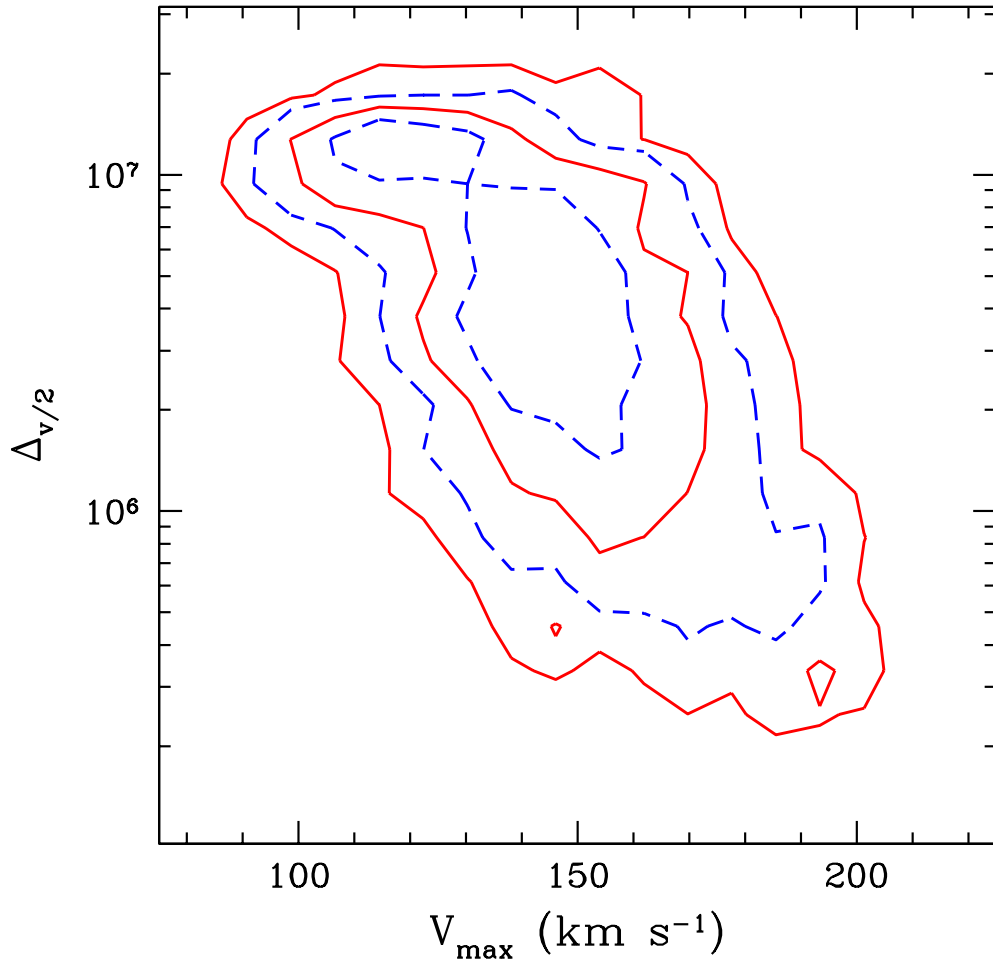


Fig. 13.— Contour plot of the probability distribution function of $\Delta_{v/2} - V_{\max}$.

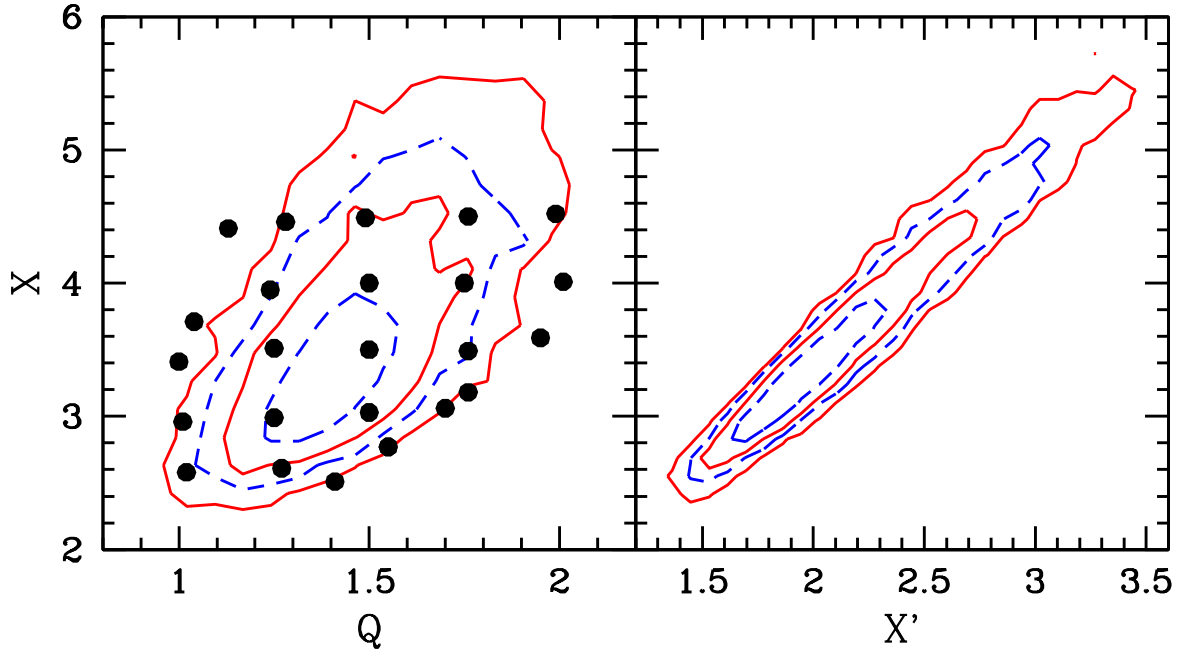


Fig. 14.— Contour plots of probability distribution function of models in the $Q - X$ and $X' - X$ planes. Solid contours enclose 68% and 95% of the models. Dots correspond to models used in bar formation study in Section 7.

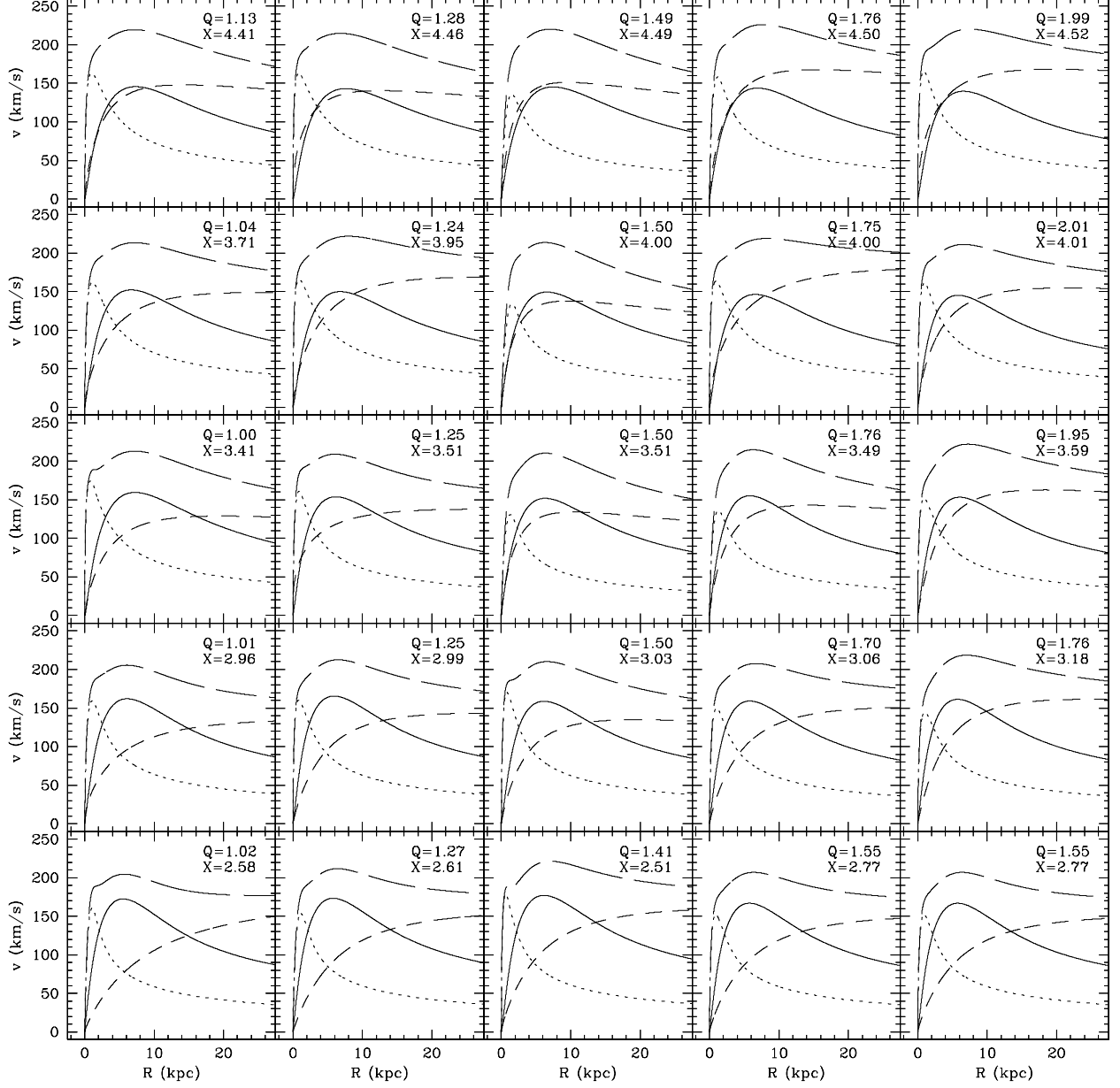


Fig. 15.— Rotation curves for the twenty-five models used in our bar formation simulations. Models are arranged so that Q increases to the right and X increases from bottom to top. Shown are the total rotation curve (long-dashed line) and contributions to the rotation curve from the disk (solid curve), bulge (dotted curve), and halo (dashed curve).

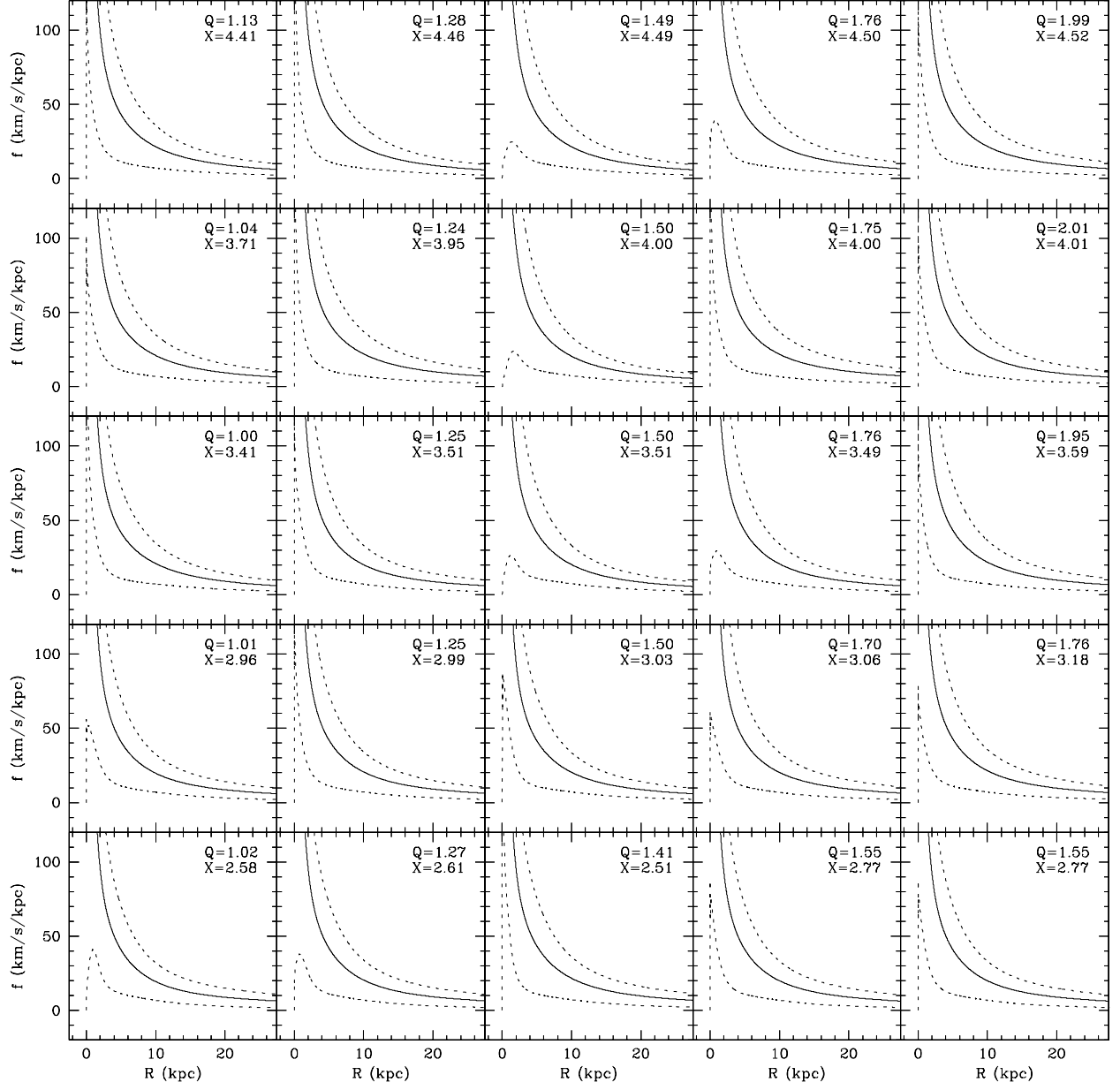


Fig. 16.— $\Omega - n\kappa/m$ as a function of radius for $n = 0$ (solid curve), $n = 1$, $m = \pm 2$ (dotted curves).

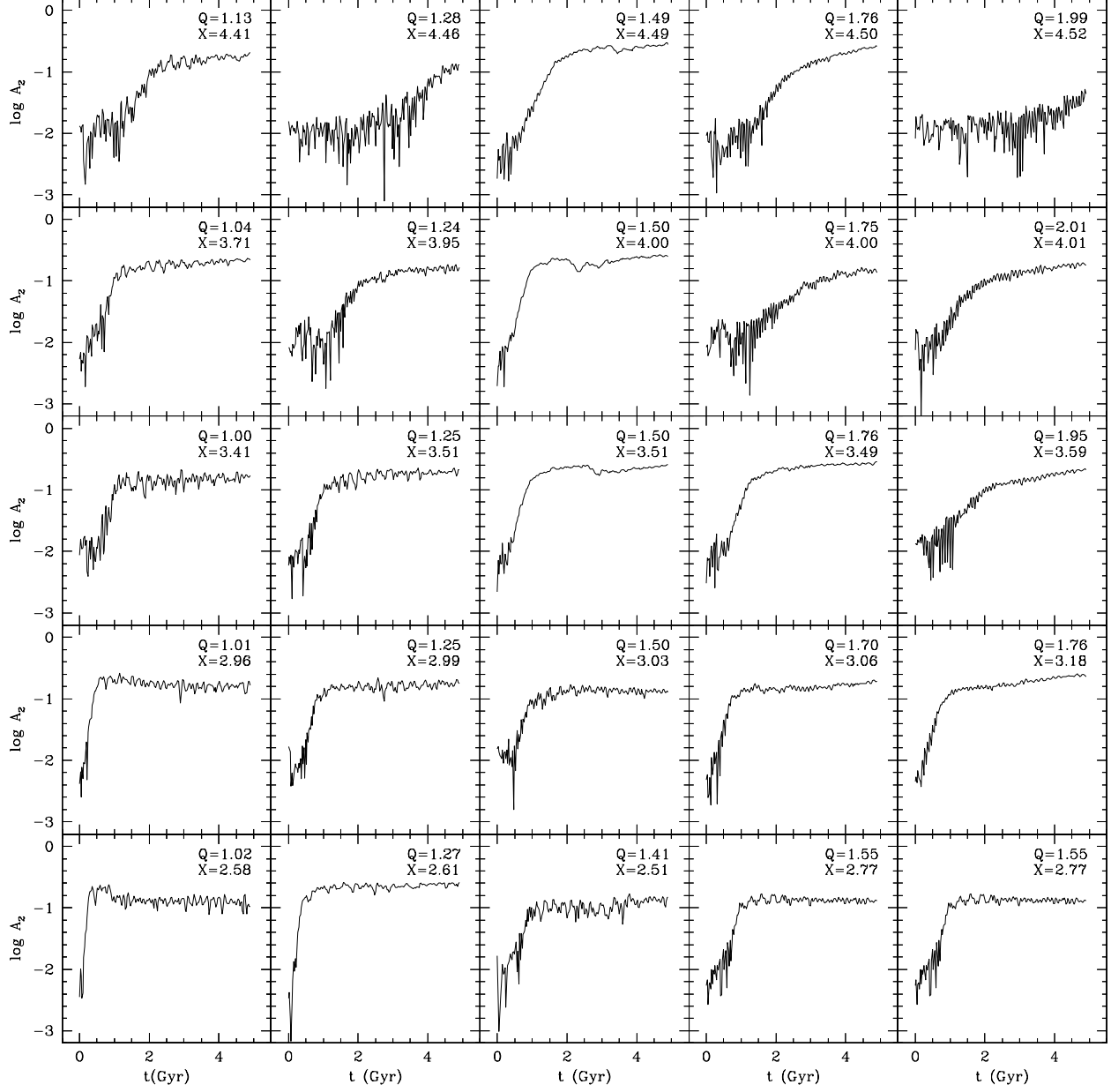


Fig. 17.— Growth of the bar strength parameter, A_2 , as a function of time.

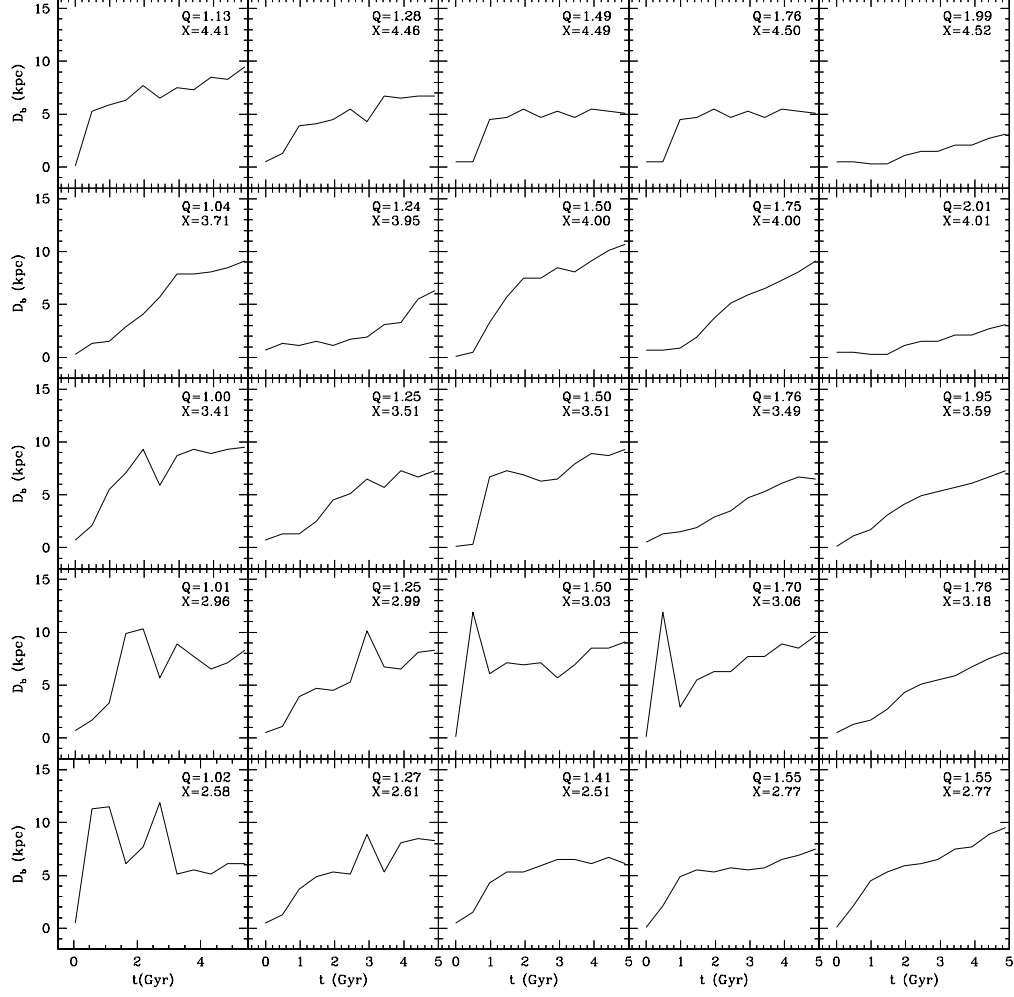


Fig. 18.— Bar length, R_b as a function of time.

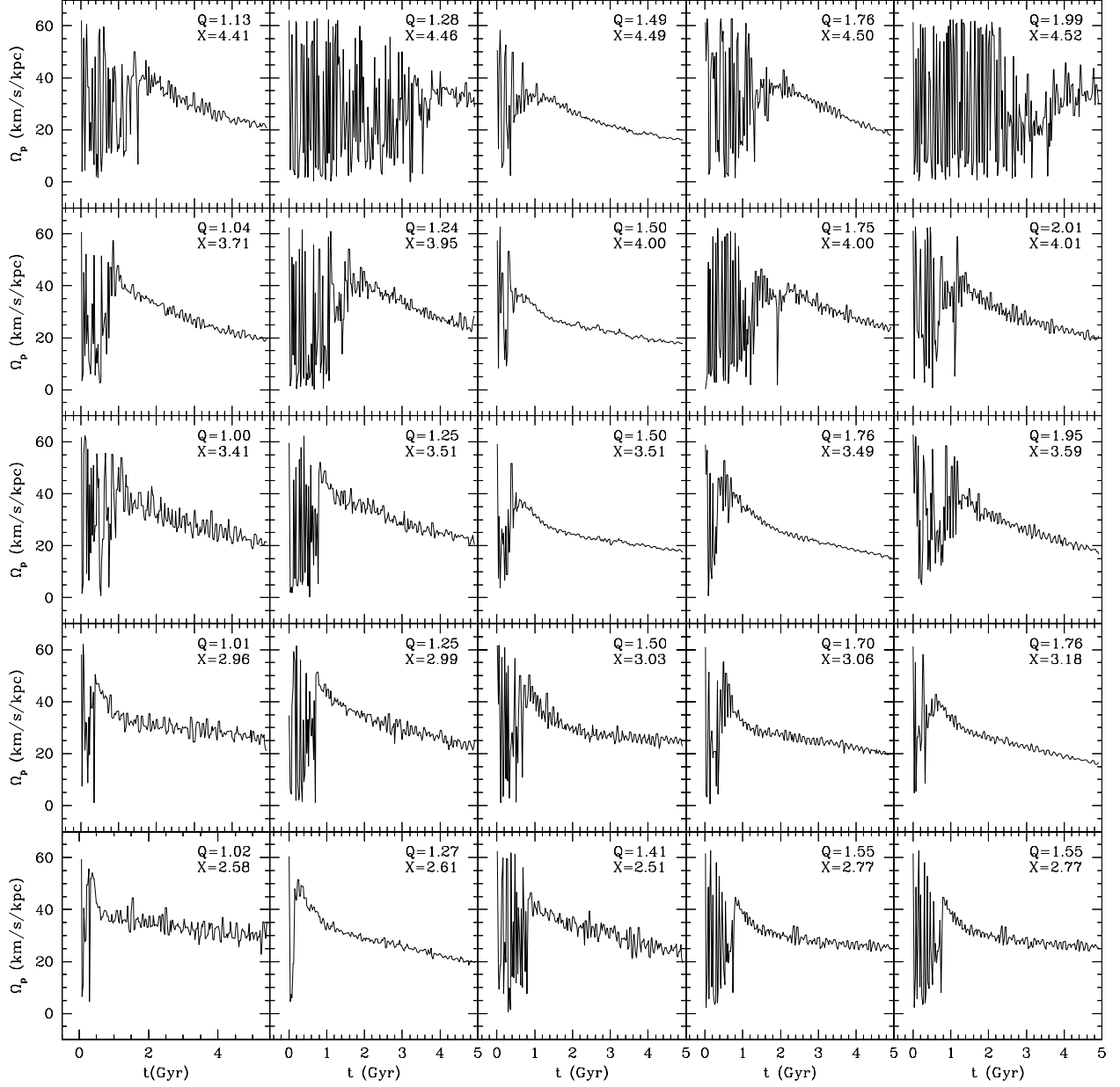


Fig. 19.— The bar pattern speed Ω_p as a function of time. Bars are born with pattern speeds $\Omega_p \sim 50 \text{ km s}^{-1} \text{ kpc}^{-1}$ which immediately begin to decay as they transfer angular momentum to halos.

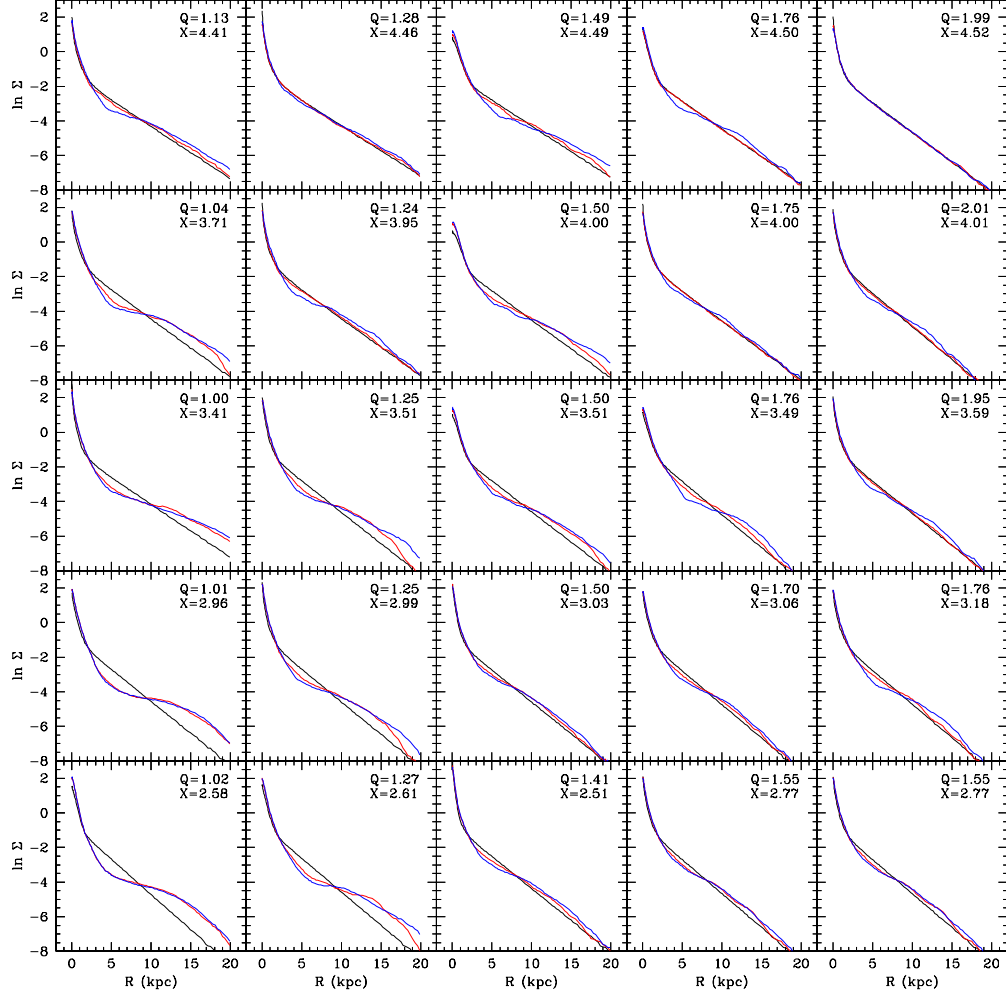


Fig. 20.— Surface density profile evolution. Three times are shown: the initial time $t = 0$ (black), $t = 2.5$ Gyr (red), and $t = 5.0$ Gyr (blue).

Table 1. model parameters and prior probabilities

parameter	prior	lower bound	upper bound
σ_h	Jeffreys	2 km s^{-1}	6 km s^{-1}
a_h	Jeffreys	2 kpc	35 kpc
γ	uniform	0	1.5
M_d	Jeffreys	$2 \times 10^{10} M_\odot$	$7 \times 10^{10} M_\odot$
R_d	Jeffreys	2 kpc	3.5 kpc
h_d	Jeffreys	0.2 kpc	1 kpc
σ_{R0}	Jeffreys	80 km s^{-1}	300 km s^{-1}
n	uniform	0.6	2.0
σ_b	Jeffreys	150 km s^{-1}	400 km s^{-1}
R_e	Jeffreys	0.4 kpc	1 kpc
$(M/L)_d$	uniform	0.6	1.2
$(M/L)_b$	uniform	0.6	1.2
R_0	Jeffreys	7 kpc	9 kpc

Table 2. results for input parameters

parameter	average
σ_h	330^{+35}_{-35}
a_h	$13.6^{+12.2}_{-9.0}$
γ	$0.81^{+0.39}_{-0.39}$
M_d	$4.1^{+0.53}_{-0.5}$
R_d	$2.8^{+0.23}_{-0.22}$
h_d	$0.36^{+0.04}_{-0.04}$
σ_{R0}	119^{+13}_{-13}
n	$1.32^{0.32}_{0.33}$
σ_b	272^{+25}_{-25}
R_e	$0.64^{+0.09}_{-0.09}$
$(M/L)_d$	$0.96^{0.1}_{0.09}$
$(M/L)_b$	$0.60^{0.07}_{0.06}$
R_0	$7.94^{0.2}_{0.2}$

Note. — Units are:
 km s^{-1} for velocities,
 $10^{10} M_\odot$ for masses, and
kpc for distances.

Table 3. results for calculated quantities

parameter	average
M_d	$4.22^{+0.52}_{-0.50}$
M_b	$0.96^{+0.12}_{-0.12}$
M_{10}	$4.23^{+0.88}_{-0.86}$
M_{25}	$12.6^{+2.9}_{-2.8}$
M_{50}	$24^{+9.4}_{-8.27}$
M_{100}	40.0^{+22}_{-19}
ρ_0	$0.0080^{+0.0014}_{-0.0014}$
σ_0	241^{+23}_{-23}

Note. — Units for ρ_0 are $M_\odot \text{pc}^{-3}$. Other quantities use the same units as in Table 2.